buildings

MDPI

Article

Dynamic Response and Mechanism Study Under Impact–Corrosion Coupling Effects

Xinping Li [1,*], Yonglai Zheng [1], Tanbo Pan [2], Yubao Zhou [3], Yong Wei [4] and Yujie Cai [4]

[1] College of Civil Engineering, Tongji University, Shanghai 200092, China
[2] College of Civil Engineering and Architecture, East China Jiaotong University, Nanchang 330013, China
[3] Faculty of Civil Engineering and Geosciences, Delft University of Technology, 2628 CN Delft, The Netherlands
[4] State Key Laboratory for Geomechanics & Deep Underground Engineering, School of Mechanics and Civil Engineering, China University of Mining and Technology, Xuzhou 221116, China
* Correspondence: 2430632@tongji.edu.cn

Abstract

Offshore reinforced concrete (RC) structures, such as bridges and high-piled wharves, are frequently subjected to the coupled action of steel corrosion and ship collision loads. However, existing studies lack systematic quantification and in-depth revelation of the synergistic degradation mechanism under this coupling effect, resulting in an insufficient scientific basis for engineering design and reinforcement. To address this gap, this study established a refined three-dimensional numerical model of drop hammer-reinforced concrete beams based on ABAQUS, comprehensively considering the strain rate effects of steel and concrete, steel–concrete bond–slip behavior, and the trilinear constitutive model of corroded steel. After validating the model's reliability against experimental data from the existing literature, parametric simulations were conducted to investigate the coupled effects of different corrosion rates and drop heights (0.25–1.5 m). Key findings include: (1) corrosion reduces the peak impact force by 9.7–58.9% and increases the maximum mid-span displacement by 6.6–35.7%, with this effect amplified by higher drop heights; (2) shear performance degradation (16.14–35.19%) is significantly more severe than flexural performance degradation (13.28–28.93%), confirming that shear performance is more sensitive to corrosion; (3) corrosion causes cracks to propagate from a localized distribution to a global distribution, while higher drop heights accelerate structural evolution toward brittle failure; (4) the synergistic degradation law of "corrosion exacerbates impact damage, and impact amplifies corrosion defects" is revealed. By quantifying the corrosion–impact coupling effect, this study advances research in the field and provides critical technical support for damage assessment and service life prediction for offshore RC structures. In engineering practice, it is recommended that offshore structures in high-corrosion environments prioritize shear resistance enhancement and adopt targeted protective measures for high-impact-risk areas to mitigate the risk of brittle failure.

Keywords: corrosion; impact force; displacement; damage; coupling mechanism

Academic Editor: Antonio Caggiano

Received: 9 February 2026
Revised: 7 March 2026
Accepted: 13 March 2026
Published: 16 March 2026

1. Introduction

Reinforced concrete (RC) structures are widely constructed due to their functional advantages and economic feasibility. However, steel corrosion stands out as one of the primary factors contributing to the deterioration of RC structures during their service life [1,2]. It not only induces early-stage structural damage but also further degrades the mechanical properties and bond strength of steel and concrete [3–5], leading to severe

deterioration in structural performance [6] and ultimately reducing the service life of structures [7]. This issue is particularly detrimental to offshore structures such as high-piled wharves and bridges constructed in chloride-rich marine humid environments. Therefore, it is crucial to consider the influence of steel corrosion when investigating the performance of in-service RC structures. In addition, ship collision is a major load source for offshore structures like high-piled wharves and bridges [8–10]. These structures inevitably suffer severe damage from ship collisions during their service life. To date, numerous accident records related to ship collisions with RC structures (e.g., bridges and high-piled wharves) have been documented [11–15]. These accidents not only cause significant physical damage to wharves and bridges but also result in substantial economic losses in the affected areas. Thus, it is necessary to investigate the dynamic characteristics and damage mechanisms of RC structures under the coupled action of steel corrosion and impact loading.

Numerous studies have been conducted on the corrosion of reinforced concrete (RC) structural members [16–18]. Apostolopoulos et al. [19] carried out artificial corrosion tests on ribbed steel bars for 10 to 120 days, revealing that corrosion duration and bar cross-sectional area significantly affect the degradation in their strength and ductility. Castel et al. [20] tested RC beams with 14 years of natural corrosion and pointed out that the "separate effect" and "coupling effect" of reduced steel cross-section and decreased bond strength are the key factors leading to the bearing capacity loss of corroded RC members. Gu et al. [21] performed flexural tests on three naturally corroded beams and nine electrochemically accelerated corroded beams, finding that with the deepening of corrosion, the short-term stiffness, yield bearing capacity, and ultimate bearing capacity of the beams all show a downward trend. Maaddawy et al. [22] investigated the influence of current densities (ranging from 100 to 500 $\mu A/cm^2$) on the electrolytic corrosion of RC structures, indicating that the electrochemically accelerated corrosion environment is most similar to natural corrosion at 200 $\mu A/cm^2$, and pitting corrosion occurs in some beams. However, the aforementioned studies mainly focused on chloride-induced steel corrosion as a single environmental factor, without considering the influence of loads borne by structural members.

Many researchers have studied the performance of concrete structures under the coupled action of load and corrosion. Padmarajaiah et al. [23] adopted the four-point bending loading method to apply loads of 1%, 8%, and 10% of the ultimate bearing capacity to concrete beams and found that the stiffness of loaded concrete beams is significantly higher than that of unloaded but corroded members. Francois et al. [24] conducted corrosion tests on RC beams under sustained load through four-point bending loading, exploring the effects of sustained stress levels and crack width on chloride ion diffusion inside the beams. Konin et al. [25] applied different levels of axial tension to concrete members with three strengths (45, 80, and 100 MPa), simulated actual working conditions by mimicking dry–wet cycles, and established a prediction model considering tensile stress levels and chloride ion diffusion coefficients. Yoon et al. [26] studied the mechanical properties of RC beams under different load levels (0–75% of the ultimate load) and different load histories (preloading and sustained loading) through four-point bending tests. Tung et al. [27] studied the influence of steel fibers on the shear strength of corroded reinforced concrete under static loads. Li et al. [28] proposed a constitutive model based on the modified compression field theory, finding that the shear strength of concrete columns decreases significantly under high corrosion rates and high axial loads. Nevertheless, the aforementioned studies mainly focused on the performance of structural members under the coupling of static load and corrosion, without considering the coupled action of dynamic load and corrosion. Relatively few studies have focused on the coupled action of corrosion and impact loading. Regarding the impact performance of corroded RC members,

drop hammer impact tests are commonly used in laboratories to investigate their dynamic responses and damage characteristics.

Regarding the coupling of dynamic load and corrosion, many scholars have also carried out relevant research. Guo et al. [29] and Yuan et al. [30] conducted tests on coastal bridge pier members under the combined action of uneven corrosion and cyclic loading, and emphasized the plastic hinge transfer mechanism of corroded bridge piers. Based on cyclic tests on beam-columns, Chinnasamy et al. [31] found that replacing cement with high-volume fly ash-engineered cementitious composites can significantly improve the bearing capacity of glass fiber-reinforced polymer (GFRP) beam-columns. Kashani et al. [32] developed an element model considering the inelastic buckling of corroded longitudinal steel bars to predict the seismic performance of RC bridge piers. Cheng et al. [33] simulated the cyclic behavior of corroded RC bridge piers considering the strain penetration effect. Xu et al. [34] evaluated the seismic failure modes and bearing capacity of corroded RC columns by means of machine learning. Miao et al. [35] used numerical simulation to study the failure mode of longitudinal steel bars under the coupling of chloride ion attack and earthquakes, observing that the structural failure mode transitions from column-type failure to beam-type failure over time. Meda et al. [36] conducted cyclic loading tests on two full-scale RC columns and found that when the steel corrosion degree reaches 20%, the ultimate deformation capacity of the columns decreases by 50%. Li et al. [37] reported the results of quasi-static cyclic tests on six RC columns, finding that uneven corrosion leads to asymmetric mechanical properties of the structure in positive and negative directions. In recent years, scholars have further expanded the research dimensions of the coupling between dynamic loads and corrosion. Li et al. [38] systematically investigated the dynamic response and failure mode of reinforced concrete beams under impact loading through a combination of experiments and numerical simulations. Wu et al. [39] conducted research on the response of corroded RC bridge piers under rockfall impact. In addition, Tran et al. [40] improved the corrosion resistance of reinforced concrete structures by adding hybrid corrosion inhibitors, providing a new material-level solution for mitigating corrosion–impact coupled damage.

However, the aforementioned studies mainly focused on quasi-static loading or low-velocity dynamic loading scenarios under cyclic loading and seismic action, with no involvement of impact loading. Although research on the performance of structural members under impact loading has been extensively carried out through drop hammer tests and finite element analysis [41–46], the influence of steel corrosion has not been considered. In terms of research on optimizing structural performance under impact loading, Li et al. [47] proposed the use of scrap steel fiber rubber concrete to improve the impact resistance of structures. Wang et al. [48] analyzed the response of corroded pipelines containing supercritical carbon dioxide ($SCCO_2$) under impact loading and found that the material performance degradation caused by corrosion significantly amplifies structural damage under impact loads. This also illustrates the necessity and engineering value of this study focusing on the quantitative analysis of such coupling effects. Cheng et al. [49] conducted a study on reinforced concrete (RC) beams and found that different impact velocities lead to distinct failure characteristics of RC beams. Daneshvar et al. [50] conducted low-velocity impact tests on corroded reinforced concrete slabs and found that corrosion damage significantly reduces the peak impact force and energy absorption capacity. When the corrosion degree reaches 15%, the energy absorption capacity decreases by 77% compared with intact specimens. Tamai et al. [51] performed drop hammer impact tests on corroded RC beams and concluded that cracks induced by corrosion are the primary factor leading to the degradation in the impact resistance of RC beams. Due to the long test cycle and high cost, Chen et al. [52] and Liu et al. [53] respectively employed numerical

simulation to investigate the influence of corrosion on the impact response of reinforced concrete (RC) columns and RC beams under impact loading.

In summary, existing research in the field of corrosion–impact coupling still has three core gaps: firstly, most studies focus on corrosion as a single factor or only consider the coupling of non-impact loads and corrosion, lacking systematic quantification of structural dynamic response indicators under the synergistic effect of dynamic impact and corrosion; secondly, the quantitative impact of corrosion on structural shear and flexural performance, as well as the differences in sensitivity, have not been thoroughly analyzed, and it is difficult to support targeted reinforcement design with existing results; thirdly, most existing numerical models fail to simultaneously integrate the synergistic effects of strain rate effects, steel–concrete bond–slip behavior, and the constitutive model of corroded steel, resulting in insufficient simulation accuracy of coupled damage and difficulty in reflecting the structural failure characteristics in real service environments. The innovation of this study is as follows: By integrating the strain rate effects of steel and concrete, the trilinear constitutive model of corroded steel, and steel–concrete bond–slip behavior, the accurate simulation of structural dynamic response and damage evolution under corrosion–impact coupling scenarios is realized, making up for the deficiency of existing models in considering multiple factors synergistically; the variation laws of various indicators and the high sensitivity of shear performance under the coupling effect of corrosion rate and impact energy are systematically quantified, and the research on dynamic damage of reinforced concrete structures is improved.

The core objective of this study is to quantify the impact force, displacement, internal force, and damage evolution characteristics of RC beams under the coupling effect of different corrosion rates (0–15%) and drop heights (0.25–1.5 m) through parametric simulations and to clarify the influence laws and inherent mechanisms of the coupling effect. Its significance lies not only in filling the gap in the quantitative analysis of coupling effects in academic research but also in providing a scientific basis for damage assessment, service life prediction, and impact-resistant reinforcement design of key infrastructure such as bridges and high-piled wharves in marine environments.

2. Materials and Methods

2.1. Overall Problem Definition

Offshore reinforced concrete (RC) structures are inevitably exposed to harsh corrosive marine environments, and dynamic loads such as ship collisions and rockfall impacts occur frequently, posing a severe threat to the safety and service life of offshore RC structures. Existing research on this coupling effect has obvious deficiencies: most studies focus on single factors such as corrosion or impact, lacking systematic examination of the structural dynamic response and damage mechanism under the synergistic action of corrosion and impact, thus failing to provide targeted technical support for engineering design and reinforcement.

To address the above research gaps and meet engineering demands, this study is dedicated to establishing a refined numerical model of RC beams under the coupling action of steel corrosion and impact loading, aiming to systematically solve the following core research problems: (1) How to integrate the strain rate effect, bond–slip behavior and constitutive model of corroded steel bars to accurately simulate the dynamic response of corroded RC beams under impact loading? (2) What are the variation laws of key dynamic response indicators (impact force, displacement, shear force, and bending moment) of RC beams under different corrosion rates and impact energy levels? (3) What is the differential degradation mechanism of the shear and flexural performance of RC beams under the

coupling effect of corrosion and impact? (4) How does the coupling of corrosion and impact affect the crack evolution and failure mode of RC beams?

Against this background, this study takes RC beams, the typical components of offshore structures, as the research object, with corrosion rates (0%, 5%, 10%, and 15%) and drop heights (0.25 m, 0.5 m, 1.0 m, and 1.5 m) as the key variables. The corrosion rate is quantified by the mass loss rate of steel bars, defined as the ratio of the mass loss of steel bars before and after corrosion to their initial mass (Figure 1). This quantification method is widely used in engineering and academic research due to its simplicity, accuracy and strong operability [22,54].

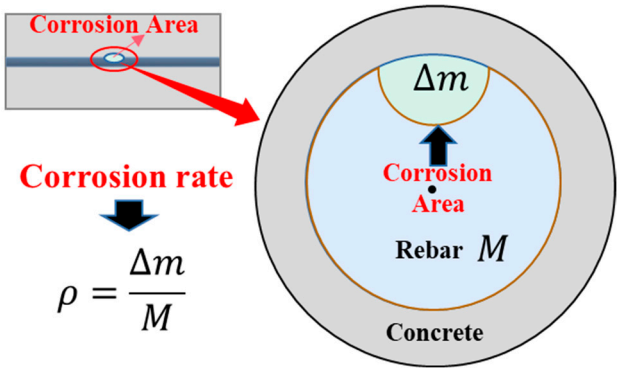

Figure 1. Sketch of rebar with corrosion.

To ensure the reliability and applicability of the research results, this study adopts a combined method of numerical simulation and experimental verification with literature data. First, experimental data are used to validate the established numerical model, including consistency verification of impact force–time history curves, displacement–time history curves and crack morphology. On this basis, parametric simulations are carried out to systematically investigate the dynamic response characteristics and damage evolution mechanism of RC beams under different corrosion–impact coupling conditions.

It should be noted that the numerical model established in this study fully considers the key factors affecting the coupling effect: (1) the strain rate effect of steel and concrete under impact loading, which is crucial for accurately simulating the dynamic mechanical properties of materials [55,56]; (2) the bond–slip behavior between steel and concrete, which directly affects the cooperative working performance of steel and concrete under dynamic loading [57]; (3) the trilinear constitutive model of corroded steel bars applicable to the corrosion rate range of 0–15%, which can accurately reflect the degradation of mechanical properties such as the yield strength and ultimate strength of corroded steel bars. The model is constructed using ABAQUS-6.14 software, and effective simulation is achieved by reasonably defining material constitutive relations, contact interactions and boundary conditions. The subsequent sections will elaborate on the modeling process in detail from the aspects of material properties, contact settings and mesh division.

2.2. The Material Constitutive Model and Material Properties of Concrete

The Concrete Damage Plasticity (CDP) model simulates the characteristic of concrete's unloading stiffness degradation with increasing strain by introducing damage variables to reduce the concrete's elastic modulus, and it can be used to simulate the mechanical behavior of RC members under dynamic loading. This model is particularly suitable for dynamic simulations like earthquakes and impact loads [58]. The CDP model uses a scalar damage degradation variable, d, to describe the stiffness degradation of concrete materials

caused by material damage, where d is a function of stress state and tensile compressive damage variables:

$$E = (1 - d)E_0 \tag{1}$$

$$(1 - d) = (1 - s_t d_c)(1 - s_c d_t) \tag{2}$$

In the formulas, d_c and d_t are the uniaxial compression and tension damage variables of concrete respectively, reflecting the unloading weakening response of concrete during the plastic strain stage under compression and tension. s_c and s_t are stress-state functions related to the recovery of tensile and compressive stiffness, which are calculated as follows:

$$s_t = 1 - w_t r^*(\sigma_{11}) \qquad 0 \le w_t \le 1 \tag{3}$$

$$s_c = 1 - w_c(1 - r^*(\sigma_{11})) \qquad 0 \le w_c \le 1 \tag{4}$$

In the formulas, w_t and w_c are the recovery factors of tensile and compressive stiffness, respectively, which control the degree of stiffness recovery of concrete during the transition from tension to compression and from compression to tension, and $r^*(\sigma_{11})$ is a uniaxial stress factor related to the principal stress state and determined as follows:

$$r^*(\sigma_{11}) = H(\sigma_{11}) = \begin{cases} 1 & \sigma_{11} > 0 \\ 0 & \sigma_{11} < 0 \end{cases} \tag{5}$$

where σ_{11} is the the first principal stress.

The stress–strain curve for concrete in the CDP model is shown in Figure 2.

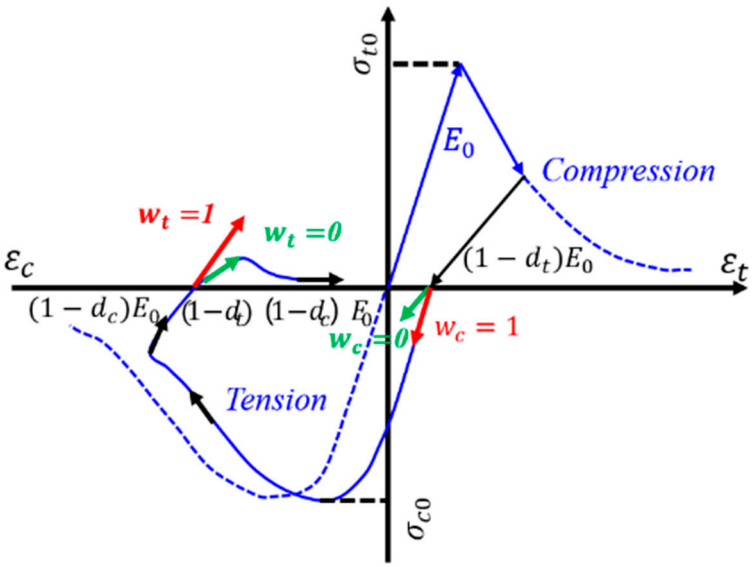

Figure 2. The stress–strain relationship of the CDP model.

In addition, the Poisson's ratio of the concrete is 0.2 and the density is 2400 kg/m^3. The value of this parameter is based on the provisions for the basic performance parameters of ordinary concrete materials specified in the Chinese Code for Design of Concrete Structures (GB 50010-2010) [59].The other plastic damage parameters for the concrete input in Abaqus-6.14 are detailed in Table 1. This set of parameters was determined with reference to the performance indicators of C30 concrete specified in the Chinese Code for Design of Concrete Structures (GB 50010-2010) [59], combined with the optimization research on the plastic damage model of corrosion-damaged concrete conducted by Hanjari et al. [60].

Table 1. Mechanical performance parameters of concrete.

Expansion Angle (°)	Eccentricity	σ_{b0}/σ_{c0}	K_c	Viscosity Parameter
30	0.1	1.16	0.66667	1×10^{-5}

Since this study focuses on impact loading, the strain rate effect of concrete must be taken into account. The dynamic parameter formulas for concrete considering the strain rate effect are as follows [55]:

$$E_{0d} = E_0\left(\frac{\dot{\varepsilon}}{\dot{\varepsilon}_{sc}}\right)^{0.002[\log(\dot{\varepsilon}/\dot{\varepsilon}_{sc})]^{1.12}} \tag{6}$$

$$f_{cd} = f_c\left(\frac{\dot{\varepsilon}}{\dot{\varepsilon}_{sc}}\right)^{0.006[\log(\dot{\varepsilon}/\dot{\varepsilon}_{sc})]^{1.05}} \tag{7}$$

$$\varepsilon_{cd} = \varepsilon_c\left(\frac{\dot{\varepsilon}}{\dot{\varepsilon}_{sc}}\right)^{-0.036+0.01\log(\dot{\varepsilon}/\dot{\varepsilon}_{sc})} \tag{8}$$

where E_0 is the initial elastic modulus for static loading; f_c is the compressive strength under static loading; ε_c is the strain corresponding to f_c; $\dot{\varepsilon}$ is the strain rate; $\dot{\varepsilon}_{sc}$ = 0.000012 (1/s); and E_{0d}, f_{cd}, and ε_{cd} are the dynamic elastic modulus, dynamic compressive strength, and dynamic compressive strain.

The dynamic tensile strength is given as follows [61]:

$$f_{td} = f_t \exp(0.00126(\log_{10}(\dot{\varepsilon}/\dot{\varepsilon}_{st})^{3.373}) \tag{9}$$

where $\dot{\varepsilon}_{st} = 10^{-7}$ (1/s) and f_t is the tensile strength under static loading.

Considering the fact that steel corrosion will cause the cracking of the concrete cover, reducing the compressive strength of the concrete, this paper introduces the concrete compressive strength reduction coefficient, ψ [62], to simulate the rust-induced cracking damage of the concrete cover. According to the suggestion by Hanjari et al. [60], the tensile strength of corrosion-damaged concrete should be reduced in proportion to the degradation in its compressive strength.

This strength reduction coefficient has been verified by studies in the literature [63–66], and the calculation model is shown as follows:

$$\psi = \frac{1}{1 + k\varepsilon_1/\varepsilon_0} \tag{10}$$

$$\varepsilon_1 = \frac{n_{bar.l}2\pi(v_{rs} - 1)x}{p_{cp}} \tag{11}$$

$$x = \frac{\phi_{sl}(1 - \sqrt{1-\rho})}{2} \tag{12}$$

where k is a coefficient related to the diameter and roughness of the steel bar, and the value is 0.1 [67]; ε_1 and ε_0 are the average tensile strain caused by the rust-induced cracking of the concrete cover and the compressive strain corresponding to the maximum stress of the uncorroded and undamaged concrete, respectively; $n_{bar.l}$ and v_{rs} are the number of all the main bars in the cross-section of the prism and the steel corrosion expansion rate (the ratio of the volume of corrosion oxides to the volume of raw materials, generally taken as 2 [54]), respectively; x and p_{cp} are the corrosion depth of the steel bar (mm) and the cross-sectional perimeter of the specimen (mm), respectively; and Φ_{sl} and ρ are the diameter of the uncorroded main bar (mm) and the mass loss rate of the main bar (%), respectively.

2.3. The Material Constitutive Model and Material Properties of Rebar

Li et al. [68] conducted simulated corrosion tests on 270 threaded rebar with different diameters by immersing them in a 5% chloride salt solution. Through methods such as high-precision weighing and tensile testing, mechanical property parameters like the corrosion rate and yield strength were accurately obtained. Based on the experimental data, it was found that when the corrosion rate of the rebar was relatively low and the yield plateau had not disappeared, the trilinear model (Figure 3a) was adopted [69]; when the corrosion rate exceeded a certain critical point of 15% [70], the strain hardening degenerated to coincide with the yield strain, the yield plateau disappeared, and the bilinear model (Figure 3b) was used.

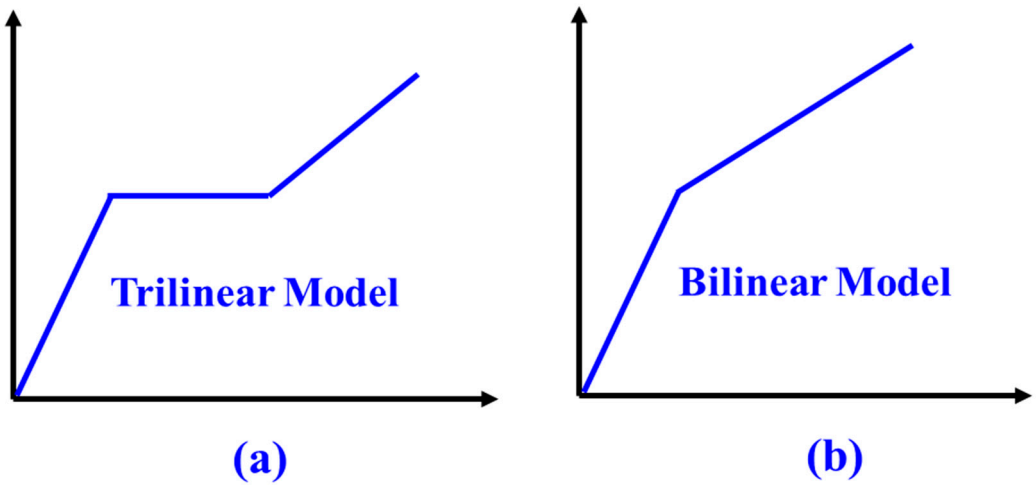

Figure 3. Trilinear constitutive model (**a**) and bilinear constitutive model (**b**) of steel rebar.

For this study, since the corrosion rate of the steel rebar in the established rebar corrosion model does not exceed 15%, the trilinear model is adopted. The steel rebar and stirrups used are HRB400, and the relevant parameters of the uncorroded steel rebar are shown in Table 2. The value of this parameter is strictly based on the provisions for the mechanical properties of HRB400 steel bars specified in the Chinese Code for Design of Concrete Structures (GB 50010-2010) [59]. Core indicators such as a yield strength of 400 MPa and an ultimate tensile strength of 540 MPa are consistent with the code requirements. Meanwhile, reference is made to the standard parameter system adopted by Wang et al. [71] and Wu et al. [72] in their research on the constitutive model of corroded steel bars, ensuring the standardization and rationality of the model parameters. The detailed constitutive model of the corroded steel rebar is shown in Figure 4. As shown in Figure 4, σ_{sc} represents the stress of the corroded steel rebar; f_{yc} and f_{uc} represent the yield strength and ultimate tensile strength of the corroded steel rebar, respectively; and ε_{sc}, ε_{shc}, ε_{suc}, E_{sc}, and E_{shc} represent the linear strain, strain hardening, ultimate strain, elastic modulus, and linear elastic modulus of the corroded steel rebar, respectively.

Table 2. The relevant parameters of the uncorroded steel rebar.

Rebar Type	Density (kg/m^3)	Elastic Modulus (GPa)	Poisson's Ratio	Yield Strength (MPa)	Ultimate Tensile Strength (MPa)
HRB400	7850	200	0.25	400	540

$$\sigma_{sc} = \begin{cases} E_{sc}\varepsilon_{sc}(\varepsilon_{sc} \leqslant f_{yc} / E_{sc}) \\ f_{yc}(\varepsilon_{shc} \geqslant \varepsilon_{sc} \geqslant f_{yc} / E_{sc}) \\ f_{yc} + E_{shc}\left[\varepsilon_{sc} - \varepsilon_{shc}\right](\varepsilon_{suc} \geqslant \varepsilon_{sc} \geqslant \varepsilon_{shc}) \end{cases}$$

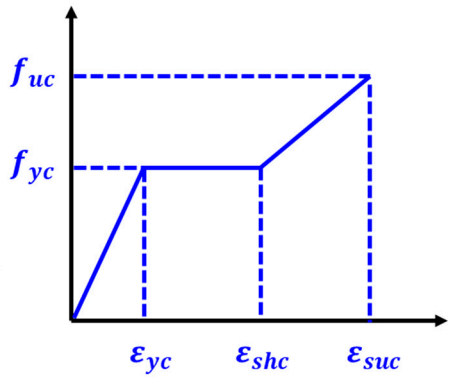

Figure 4. Detailed trilinear constitutive model of corroded steel rebar.

For steel bars under impact loading, the strain rate effect amplification factor is typically used for calculations [56]:

$$\frac{f_d}{f_s} = (\frac{\dot{\varepsilon}}{10^{-4}})^{\delta} \tag{13}$$

where f_d is the dynamic strength of the steel bar; f_s is the static strength of the steel bar; for the ultimate strength, $\delta = 0.019 - 0.009 f_y/414$; for the yield strength, $\delta = 0.074 - 0.040 f_y/414$; and f_y is the yield strength of the steel bar (MPa).

The nominal yield strength and nominal elastic modulus of a corroded rebar are computed utilizing the model developed by Wang and Liu [71]:

$$f_{yc} = (1 - 0.00198\rho) f_y \tag{14}$$

$$E_{sc} = (1 - 0.00113\rho) E_s \tag{15}$$

In these formulas, f_y represents the nominal yield strength of the rebar before corrosion, E_s denotes the nominal elastic modulus of the rebar before corrosion, and ρ is the corrosion rate.

To calculate the ultimate strength and ultimate strain, the model proposed by Wu and Yuan is employed [72]:

$$f_{uc} = (1 - 0.0019\rho) f_u \tag{16}$$

$$\varepsilon_{suc} = (1 - 0.021\rho) \varepsilon_u \tag{17}$$

where f_u is the nominal ultimate strength of the rebar before corrosion and ε_u is the nominal ultimate strain of the rebar before corrosion.

In addition, to ensure the accuracy of the finite element simulation, this paper considers the bond–slip behavior between steel bars and concrete with reference to Chinese codes, as shown in Figure 5. Meanwhile, this study establishes a reduction calculation formula for bond strength considering the corrosion of both stirrups and longitudinal reinforcement [60].

2.4. Contact Interaction and Element Meshes

The specimens used in the numerical simulation are based on the relevant specimen information from References [73,74]. The geometric dimensions of the cross-section and the plan view of the reinforcement arrangement of the RC beam are shown in Figure 6a, and a 3D view of the reinforcement cage is presented in Figure 6b. The cross-sectional dimensions of the reinforced concrete beam are 200 mm × 200 mm, with the longitudinal reinforcement consisting of 4 D16 bars and the transverse stirrups being D10@100, and the beam length is 1800 mm. The overall model includes key components such as a 400 kg drop

hammer (for applying impact loads), the RC beam specimen, longitudinal reinforcement, stirrups, rigid supports (for simulating boundary conditions), and spacers (for ensuring the positioning of reinforcements), as shown in Figure 7.

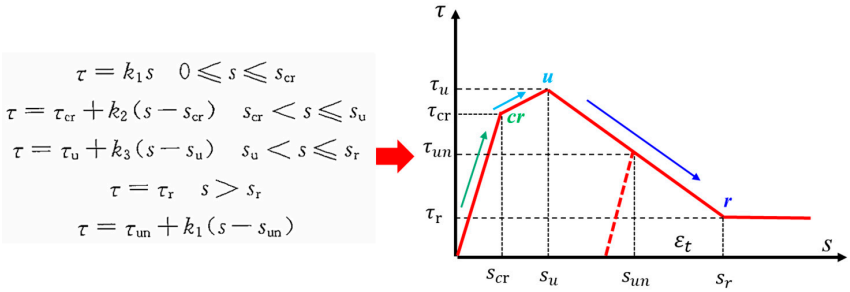

Characteristic Point	Splitting (cr)	Peak (u)	Residual (r)
Bond Stress (N/mm²)	$\tau_{cr} = 2.5 f_{t,r}$	$\tau_u = 3.0 f_{t,r}$	$\tau_r = f_{t,r}$
Relative Slip (mm)	$s_{cr} = 0.025d$	$s_u = 0.04d$	$s_r = 0.55d$
d is the diameter of the steel bar (mm), f is the tensile strength of concrete.			

Figure 5. Steel–concrete bond–slip constitutive model.

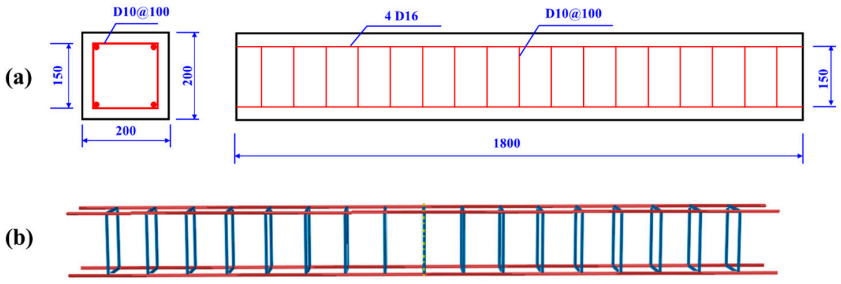

Figure 6. RC beam configuration: (**a**) cross-section view; (**b**) 3D view (unit: mm).

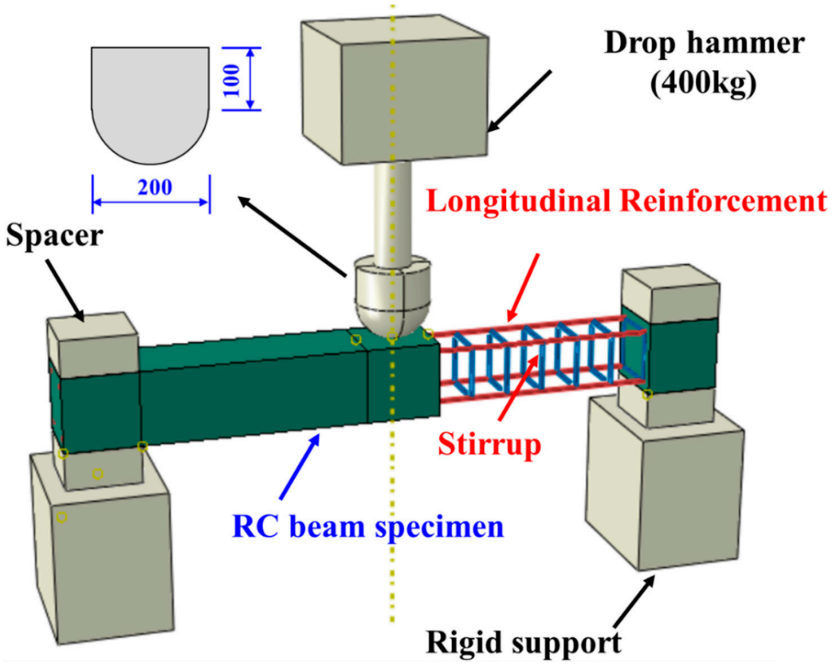

Figure 7. Detailed overall numerical simulation model.

Drop hammer mass (400 kg): Consistent with the drop hammer configuration in the physical impact tests on reinforced concrete beams conducted by Fujikake et al. [73], this

mass parameter is widely used in medium-energy impact tests on reinforced concrete beams. It can effectively induce typical dynamic damage such as flexural–shear cracking and concrete spalling of reinforced concrete beams.

Rigid support conditions: The rigid supports fully constrain the horizontal displacement and rotation at both ends of the beam, allowing only vertical deformation. This setting replicates the boundary conditions of simply supported beams in the referenced physical tests [74], serving as a standard boundary configuration for impact tests on reinforced concrete beams to eliminate the interference of additional constraints on dynamic responses. Meanwhile, this support mode is basically consistent with the actual basic support conditions of offshore reinforced concrete structural components (e.g., local beam segments of high-piled wharves), ensuring the engineering relevance of the simulation.

The setting of spacers is considered based on the actual force-bearing conditions of simply supported beams and with reference to the boundary constraints of physical tests [74]. It ensures the consistency of structural geometric parameters between the numerical model and the test conditions, laying a reliable foundation for the subsequent comparison and verification between simulation results and test data.

In the ABAQUS-6.14 interaction module, the "surface-to-surface contact" method was employed to establish the hammer–concrete interface model. To simulate the normal contact behavior between a hammer and concrete, the "hard contact" option within the "interaction properties" module was chosen. Regarding the tangential contact of the model, to study the influence of potential tangential behaviors on this problem, we used a penalty function contact in ABAQUS for solving. The penalty function specified in Equation (18) was utilized to mimic the sliding behavior [75].

$$\tau_0 = \mu P \tag{18}$$

where τ_0 is the frictional stress, μ is the friction coefficient, and P is the normal stress on the contact surface.

To avoid the impact of mesh quality on calculation results, the quadrilateral element C3D8R was used for meshing concrete and other solid components, while T3D2 elements were employed for meshing reinforcing bars and stirrups, aiming to obtain more accurate calculation results. It should be noted that to balance calculation accuracy and efficiency, and considering the precision of bond–slip between steel bars and concrete, the mesh size of the boundary regions of the main components was uniformly set to 25 mm [49] (Figure 8a). Meanwhile, to ensure that the final mesh size was sufficiently small and free of distortion, mesh quality verification was completed using the "Mesh Verify" module in ABAQUS. Figure 8b shows the complete process of meshing for the full 3D model, covering the meshing of each main component and the mesh morphology of the overall model.

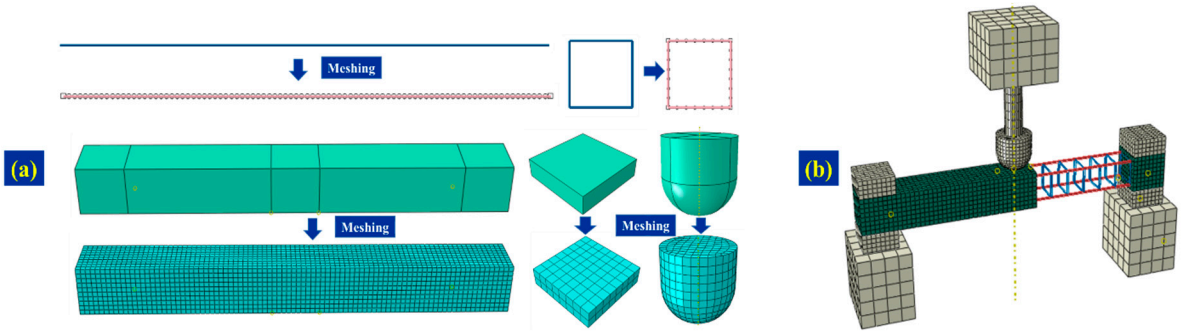

Figure 8. The entire meshing process of the overall model (**a**) Mesh generation of each component (**b**) overall effect.

3. Results

3.1. Impact Force

To verify the accuracy of the numerical simulation, a comparison with experimental results from the literature was conducted, as shown in Figure 9, which presents the comparison of the numerical simulation results and experimental results of impact force time–history curves. It should be noted that there are slight differences between the drop hammer heights adopted in the numerical simulation (0.25 m, 0.5 m, 1.0 m, and 1.5 m) and those in the referenced experiments [73] (0.3 m, 0.6 m, and 1.2 m). This inconsistency arises because this study retained the systematic drop hammer height settings to avoid disrupting the parameter gradient by scattered adjustments of individual drop hammer heights. Meanwhile, the validity of the comparison is ensured by quantifying the resulting differences in impact kinetic energy. Specifically, the kinetic energy difference for each group of comparative working conditions is calculated to be approximately 16%. Despite the aforementioned kinetic energy difference, the numerical simulation impact force time–history curves at heights of 0.25–1.0 m still exhibit good consistency in variation trends with the experimental curves (Figure 9a–c): both can accurately reflect the dynamic evolution law of impact force. In the initial stage of impact, both the simulation and experiment show a sharp increase in impact force to the peak value followed by entry into the fluctuation and attenuation stage. In addition, the inherent law that "peak impact force increases with the rise in drop hammer height" is consistently reflected in both the simulation and the experiment: the peak impact force at the 1.5 m height in the simulation (Figure 9d) is significantly higher than that at the 0.25 m height (Figure 9a), which is basically consistent with the trend of peak force increasing with drop hammer height and the peak values in the experiment [74]. In summary, this numerical model can reliably simulate the dynamic response of reinforced concrete beams under impact loads.

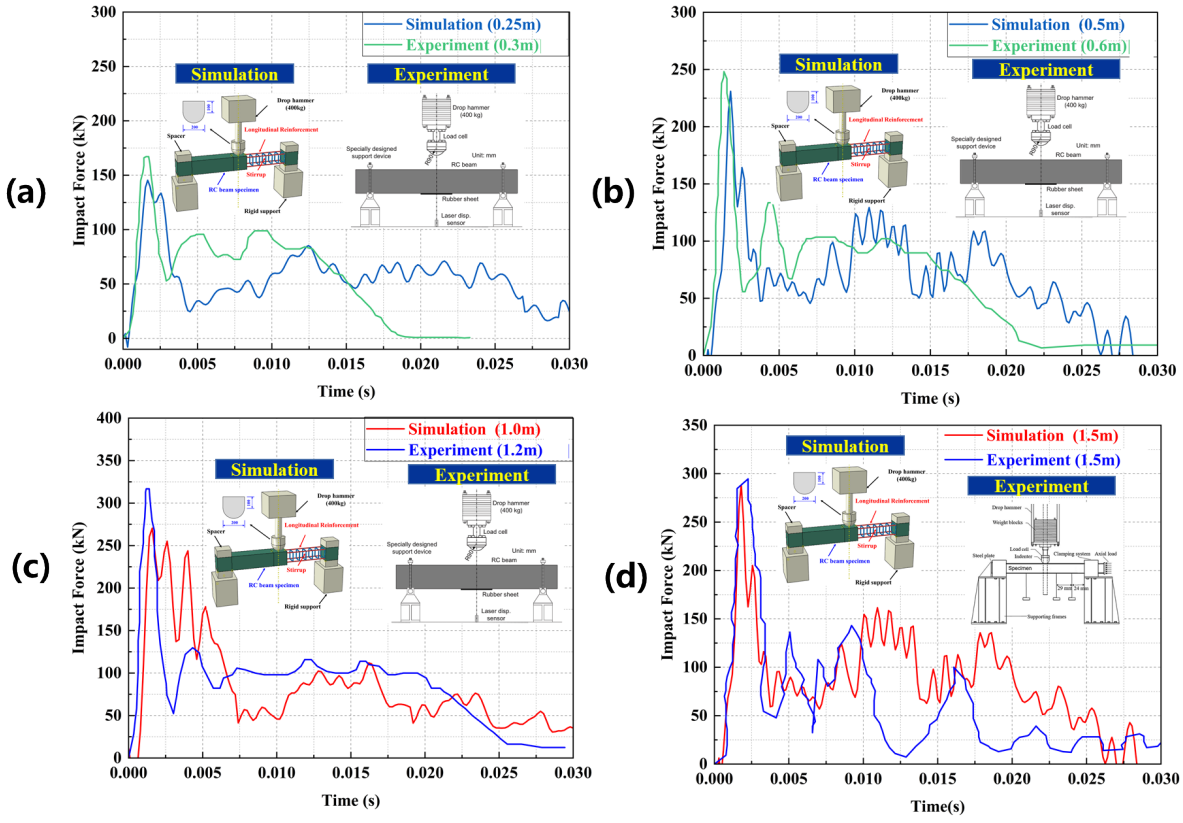

Figure 9. Time–history curves for impact force under different drop hammer heights: (**a**) 0.25 m; (**b**) 0.50 m; (**c**) 1.0 m; (**d**) 1.5 m.

Figure 10 presents the time–history curves for impact force corresponding to different drop hammer heights under various corrosion rates. It can be seen from Figure 10a–d that the increase in corrosion rate significantly changes the time–history characteristics of impact force:

1. When the corrosion rate is 0% (no corrosion), the peak impact force is highest, and the fluctuation and attenuation process of the force is more "ductile", reflecting that the uncorroded reinforced concrete structure has strong bearing and energy dissipation capacities under impact.
2. As the corrosion rate increases (5%, 10%, and 15%), the peak impact force shows a significant downward trend, and the attenuation speed of the force accelerates. For example, under the condition of a drop hammer height of 1.5 m (Figure 10d), the peak impact force at a corrosion rate of 15% is much lower than that at a corrosion rate of 0%. This is because steel corrosion leads to section loss and mechanical property degradation of steel bars, and at the same time, the bond performance between steel bars and concrete deteriorates, which greatly reduces the dynamic response capacity of the structure under impact.

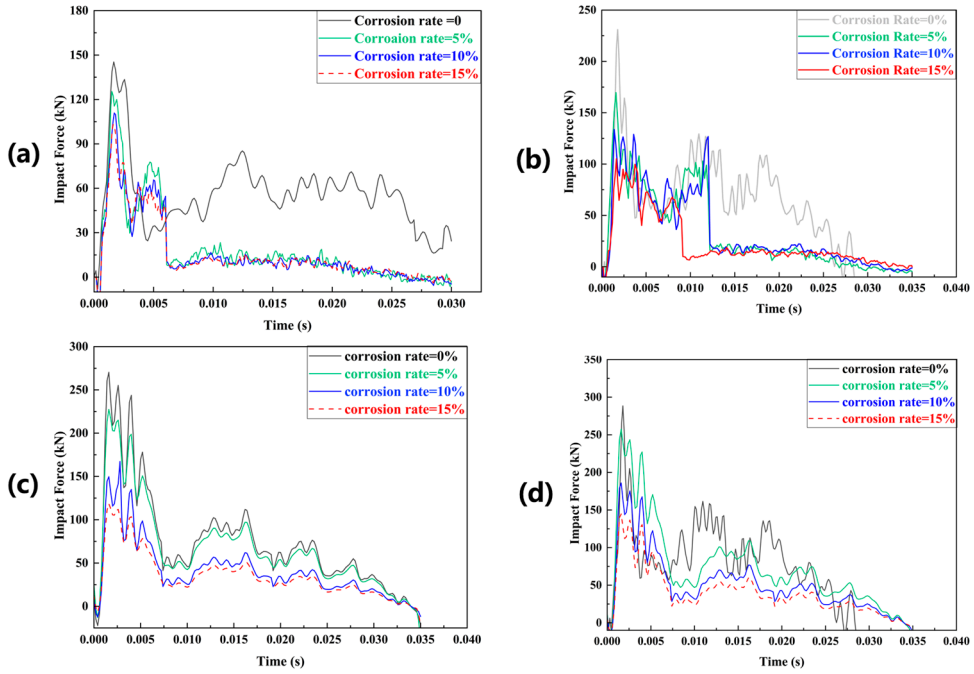

Figure 10. The time–history curves for impact force corresponding to different drop hammer heights ((**a**) 0.25 m, (**b**) 0.50 m, (**c**) 1.0 m, and (**d**) 1.5 m) under various corrosion rates.

In addition, by comparing the curves under different drop hammer heights (0.25 m, 0.5 m, 1.0 m, and 1.5 m), it can be seen that the higher the drop hammer height, the more significant the negative impact of corrosion rate on impact force. At a low drop hammer height (such as 0.25 m, Figure 9a), the peak difference of curves with different corrosion rates is relatively small; while at a high drop hammer height (such as 1.5 m, Figure 9d), the peak gap between the curve with a corrosion rate of 15% and the curve without corrosion is very large, indicating that under high-energy impact conditions, the degradation in structural performance caused by corrosion has a more prominent weakening effect on impact response. Meanwhile, the increase in drop hammer height amplifies the correlation effect of "corrosion–dynamic response". At a high drop hammer height, each increase of a certain proportion in corrosion rate leads to a more obvious decrease in the peak impact force, reflecting that the coupling effect of the two has "positive correlation amplification".

Figures 11 and 12 analyze the coupling effect of corrosion rate and impact height on the peak impact force from different dimensions. Figure 10 shows the relationship between different corrosion rates and peak impact forces. It can be seen from Figure 10a–d that under different drop hammer heights, the peak impact force decreases monotonically as the corrosion rate increases (0%, 5%, 10%, and 15%). For example, in Figure 10a, when the corrosion rate increases from 0% to 15%, the peak impact force decreases from 145.3414 kN to 103.1057 kN, with an attenuation amplitude of 29.1%; in Figure 10d, the peak value decreases from 288.4 kN to 144.76 kN, with an attenuation amplitude of 49.8%. The high goodness-of-fit of the fitting function also indicates that the linear negative correlation between corrosion rate and peak impact force is statistically significant, which can serve as the basis for the "corrosion–peak force" prediction model. Meanwhile, under high-energy impact, the degradation in structural performance caused by corrosion has a more prominent weakening effect on the peak force; that is, the increase in drop hammer height amplifies the correlation effect of "corrosion–dynamic response", which is consistent with the law shown in Figure 10.

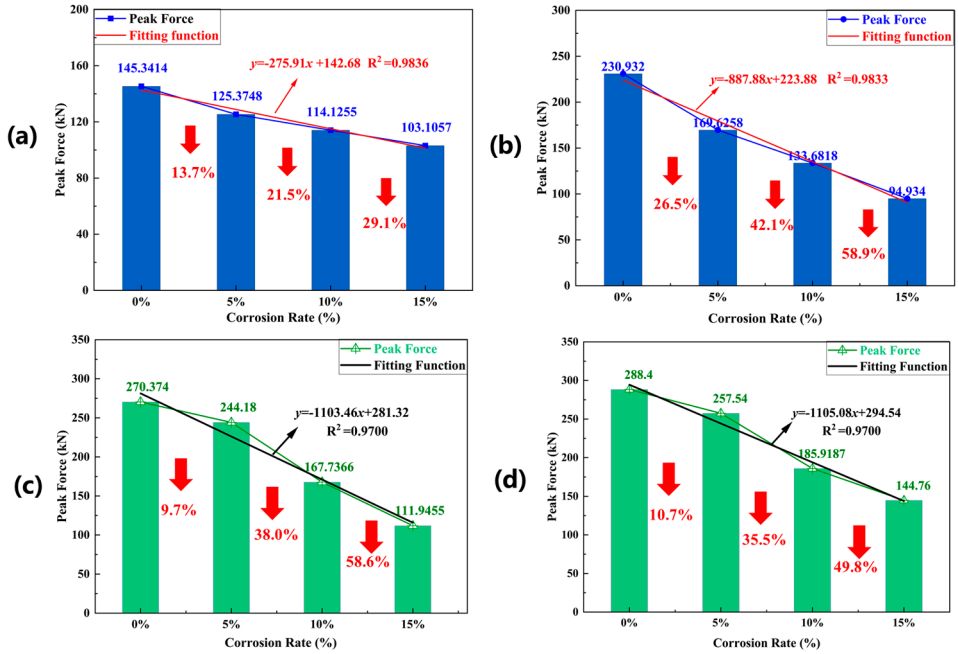

Figure 11. Relationship between corrosion rate and peak impact force under different drop hammer heights: (**a**) 0.25 m; (**b**) 0.50 m; (**c**) 1.0 m; (**d**) 1.5 m.

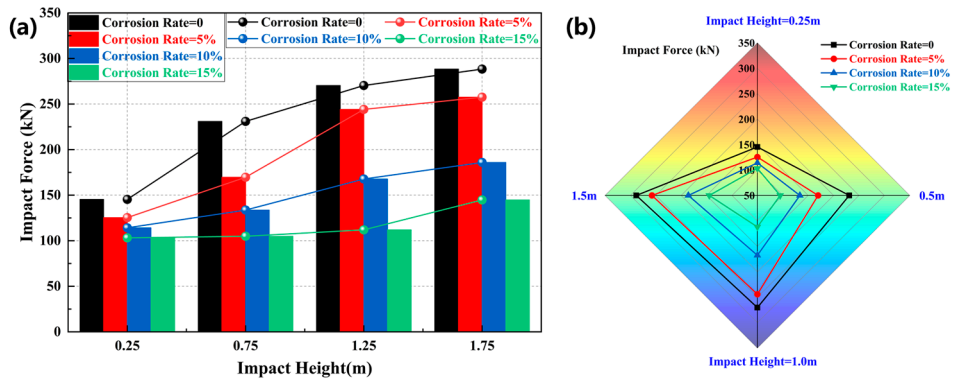

Figure 12. Comparison of peak impact force under different steel corrosion rates and impact heights: (**a**) column–dot line graph; (**b**) 3D radar graph.

Figure 12 further shows the coupling effect of corrosion rate and impact height: in the bar–line chart of Figure 12a, the curves with different corrosion rates all show an upward trend as the impact height increases (0.25 m, 0.75 m, 1.25 m, and 1.75 m), reflecting the positive contribution of impact height to the peak impact force; at the same time, under the same impact height, the higher the corrosion rate, the lower the peak force, intuitively showing the coupling effect of "negative regulation by corrosion rate and positive regulation by impact height". The radar chart in Figure 12b takes impact heights (0.25 m, 0.5 m, 1.0 m, and 1.5 m) as dimensions, and the difference in polygon area for different corrosion rates clearly reflects that "the higher the corrosion rate, the more significant the three-dimensional attenuation of the structural impact resistance". For example, the polygon area corresponding to a corrosion rate of 15% is much smaller than that corresponding to a corrosion rate of 0%, and the attenuation is most prominent in the direction of high impact height (1.5 m), which again confirms that the adverse effect of corrosion is amplified under high-energy conditions.

3.2. Displacement

Figure 13 presents a comparison of the numerical simulation results and experimental data from the literature [73,74] regarding the mid-span displacement time–history curves for reinforced concrete beams under different drop hammer heights (0.25 m, 0.5 m, 1.0 m, and 1.5 m). As illustrated in Figure 13a–d, the numerical simulation curves exhibit good consistency with the experimental curves in terms of displacement development trends across all tested drop hammer heights. Both can accurately reflect the temporal evolution law of displacement. Specifically, in the initial stage of impact, the displacement of both the simulation and experiment rises rapidly to the peak value, followed by entry into a slow attenuation stage.

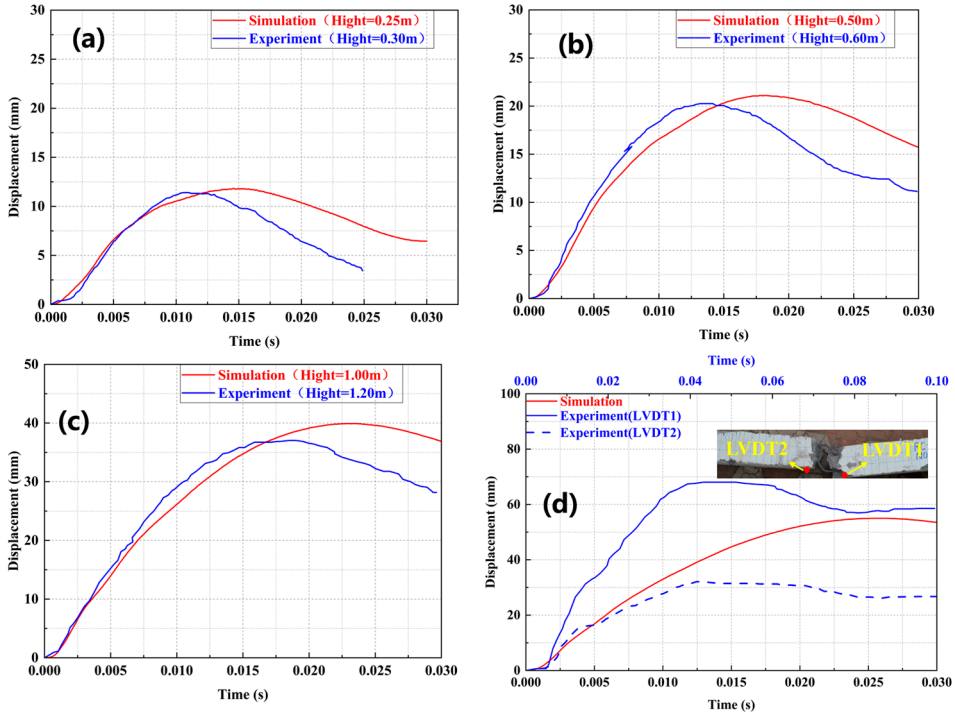

Figure 13. Comparison and verification of displacement time–history curves under different drop hammer heights: (**a**) 0.25 m; (**b**) 0.50 m; (**c**) 1.0 m; (**d**) 1.5 m.

It is worth noting that the main errors between the simulation and experimental results may also stem from the following factors: (1) differences in the cross-sectional dimensions of the specimens; (2) variations in stirrup ratios (the experimental specimens have a higher

stirrup ratio, which strengthens the constraint effect on concrete and reduces deformation); (3) discrepancies in boundary conditions between the experiment and numerical simulation; (4) minor differences in drop hammer heights. These factors collectively contribute to slight quantitative deviations between the simulation and experimental curves, but they do not affect the consistency of the overall response trends. This verifies the reliability of the numerical model in simulating displacement characteristics under different impact energy levels.

Figure 14 presents the displacement time–history curves corresponding to different corrosion rates under various drop hammer heights. It can be seen from Figure 14a–d that regardless of the drop hammer height, as the corrosion rate increases, the peak displacement shows an obvious upward trend, and the attenuation rate of displacement slows down. Under the same drop hammer height, it can be clearly found that as the corrosion rate increases, the peak displacement also increases significantly, and the occurrence of the peak value in the specimen is "delayed". For example, under the condition of a drop hammer height of 1.5 m (Figure 14d), both the peak displacement and its occurrence time at a corrosion rate of 15% are greater than those at a corrosion rate of 0%. This is because corrosion leads to a significant decrease in the mechanical properties of the reinforced concrete structure, and at the same time, the bond performance between steel bars and concrete deteriorates, which greatly reduces the deformation constraint capacity of the structure under impact, thus resulting in an increase in peak displacement and an extension of the deformation duration. In addition, it is worth noting that under the same corrosion rate, the peak displacement and its occurrence time also increase with the increase in the drop hammer height. This is because the corroded structure, due to the degradation of material and interface properties, cannot effectively dissipate high-energy impact and can only dissipate energy through "larger deformation and longer duration". Therefore, the peak displacement increases significantly with the increase in the drop hammer height, and the occurrence time of the peak value is "delayed". This is basically consistent with the variation law presented in References [52,53].

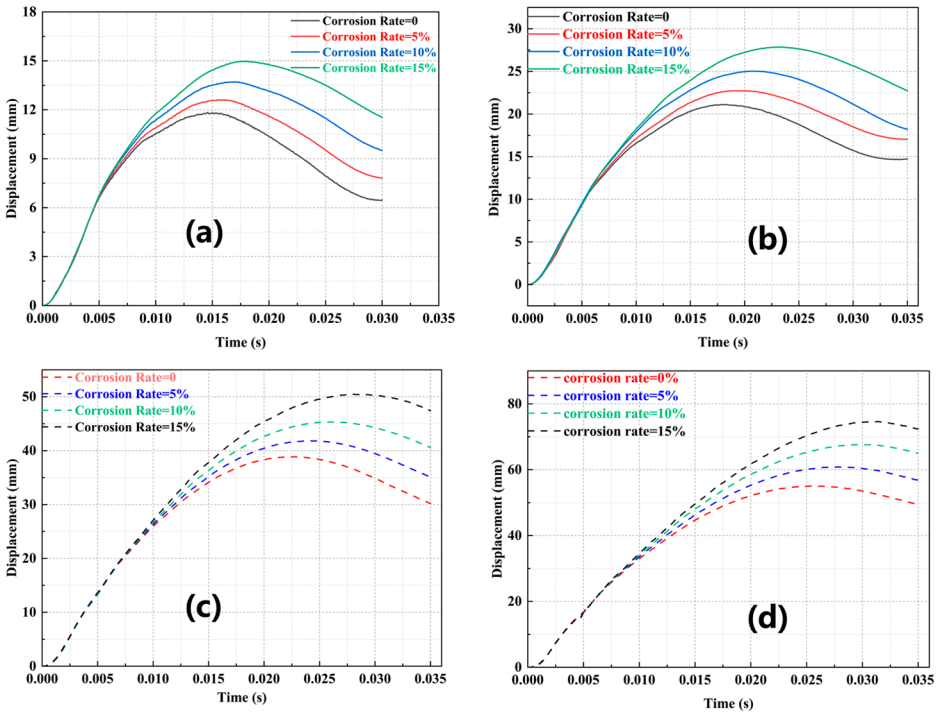

Figure 14. Time–history curves for displacement with different corrosion rates under different drop hammer heights: (**a**) 0.25 m; (**b**) 0.50 m; (**c**) 1.0 m; (**d**) 1.5 m.

Figure 15 shows the mid-span peak displacement and its rate of change for reinforced concrete beams with different corrosion rates under various drop hammer heights. It can be seen from Figure 15a–d that the peak displacement and its rate of change increase monotonically as the corrosion rate increases (0%, 5%, 10%, and 15%). For example, in Figure 15d, when the corrosion rate increases from 0% to 15%, the peak displacement increases from 55.0168 mm to 74.6553 mm, with an increase of 35.7%; at a low corrosion rate (5%), the increase is 10.6%, and at a high corrosion rate (15%), the increase expands significantly, reflecting that "the higher the corrosion rate, the more obvious the acceleration of peak displacement growth". In addition, it can be seen that the higher the drop hammer height, the more significant the influence of corrosion rate on the peak displacement: under a low drop hammer height (0.25 m, Figure 14a), the rate of change of peak displacement at a corrosion rate of 15% is 26.6%; under a high drop hammer height (1.5 m, Figure 15d), the corresponding rate of change at the same corrosion rate reaches 35.7%. This difference obtains because under the high-energy impact caused by the increase in drop hammer height, the material performance degradation of the corroded structure is further amplified, resulting in a significant expansion of the increase range of peak displacement with the increase in drop hammer height, that is, the drop hammer height has a positive correlation amplification effect on the relationship between "corrosion rate–peak displacement". It is worth noting that the rate of change increases in a "stepwise" fashion for every 5% increase in corrosion rate (for example, under a height of 0.25 m, the rates of change corresponding to corrosion rates of 5% → 10% → 15% are 6.6% → 15.9% → 26.6%); under a high drop hammer height, this "stepwise" increase is more obvious (for example, under a height of 1.5 m, the rates of change corresponding to corrosion rates of 5% → 10% → 15% are 10.6% → 22.9% → 35.7%). This may be because the weakening of the structural deformation constraint capacity by corrosion is "nonlinearly accelerated", and the high-energy input from the drop hammer height will enhance this nonlinear characteristic.

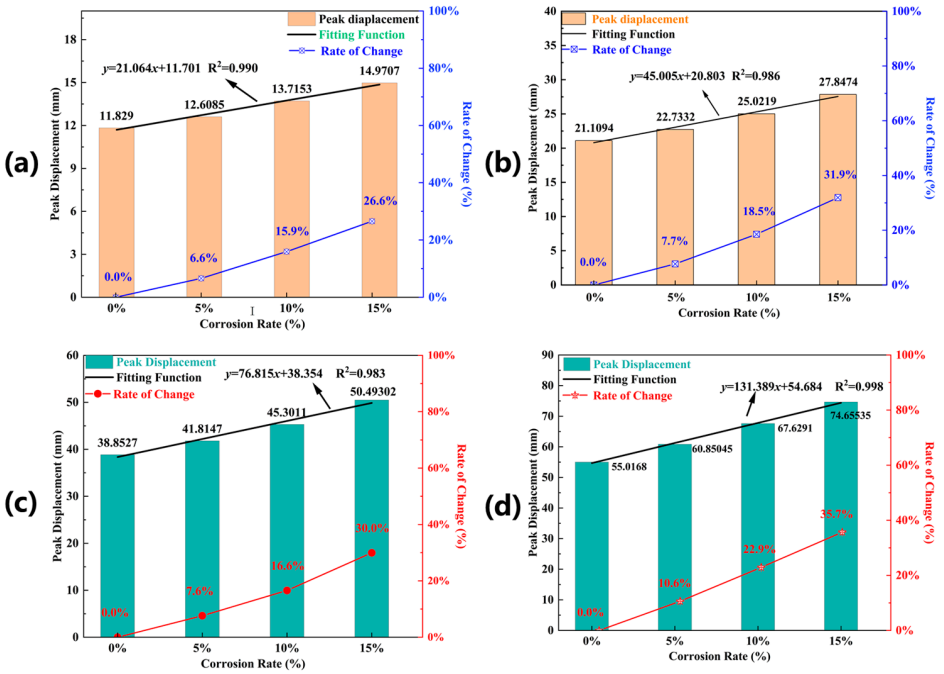

Figure 15. Mid-span peak displacement and its rate of change for reinforced concrete beams with different corrosion rates under various drop hammer heights: (**a**) 0.25 m; (**b**) 0.50 m; (**c**) 1.0 m; (**d**) 1.5 m.

Figure 16 shows the coupling effect of different impact heights and corrosion rates on the mid-span peak displacement of reinforced concrete beams. It can be seen from

Figure 16a that the peak displacements at different corrosion rates all increase monotonically with the increase in impact height (0.25 m, 0.5 m, 1.0 m, and 1.5 m), and under the same impact height, the higher the corrosion rate, the larger the peak displacement. For example, at an impact height of 1.5 m, the peak displacement at a corrosion rate of 15% is much higher than that at a corrosion rate of 0%, which indicates that "the higher the corrosion rate, the more significant the three-dimensional degradation of structural deformation", confirming the amplifying effect of corrosion on peak displacement under high-energy conditions.

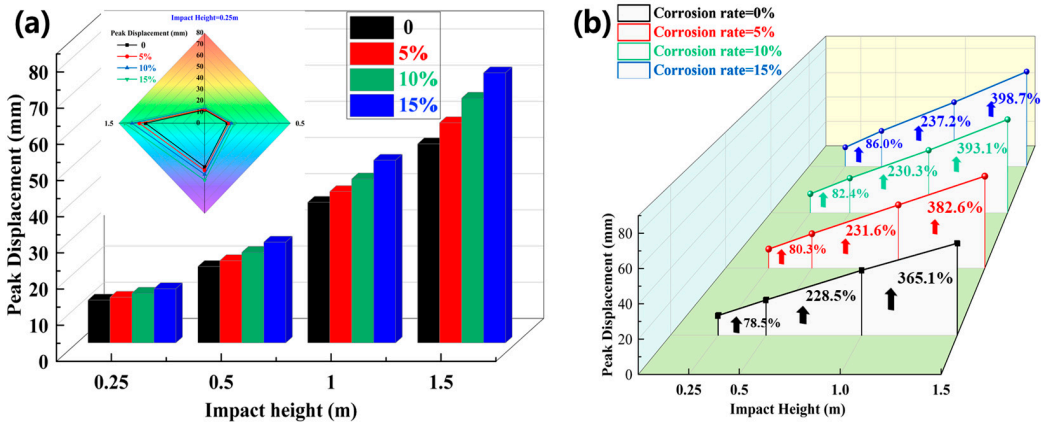

Figure 16. The coupling effect of different impact heights and corrosion rates on the mid-span peak displacement of reinforced concrete beams (**a**) bar-radar combined graph (**b**) three-dimensional line graph.

Figure 16b shows the quantification and "stepwise" degradation characteristics of the peak displacement increase. For example, at a corrosion rate of 5%, the peak displacement increases by 230.5% when the impact height increases from 0.25 m to 1.5 m. Under the same corrosion rate, the peak displacement increase shows a "stepwise" growth with the increase in impact height (for example, at a corrosion rate of 0%, the increase gradually expands as follows: 78.4% → 231.6% → 365.1%). In addition, under the same impact height, the higher the corrosion rate, the more significant the increase (for example, at an impact height of 1.5 m, the increase of 394.7% at a corrosion rate of 15% is much higher than 365.1% at a corrosion rate of 0%), reflecting the amplifying effect of corrosion on the relationship between "impact height–peak displacement", which is consistent with the previous analysis.

In the comparison of the simulation and experimental results for force and displacement responses, there exist slight discrepancies in the peak displacement and variation path. The specific reasons for these discrepancies are analyzed as follows:

(1) Influence of discrepancies in cross-sectional dimensions and reinforcement ratio: Compared with the test, the reduced beam cross-sectional dimensions in the numerical model lead to a decrease in the compression zone area of concrete, and the lower reinforcement ratio weakens the tensile stiffness of the structure. The combined effect of these two factors makes the overall stiffness of the simulated specimen slightly lower than that of the experimental specimen, resulting in deviations.

(2) In the experiment reported in Reference [73], the drop hammer heights were set at 0.3 m, 0.6 m, and 1.2 m, while the drop hammer heights adopted in the simulation of this study are 0.25 m, 0.5 m, 1.0 m, and 1.5 m. The differences in drop hammer height (and even drop hammer mass) between the numerical simulation and physical experiments mainly stem from the fact that at the initiation stage of this study, priority was given to referencing experimental data from multiple studies [53,73,74,76].

There are inherent discrepancies in the test device parameters (drop hammer mass: 400–450 kg; drop hammer height: 0.3–1.2 m) across different studies. To construct a unified "corrosion rate–drop hammer height" coupling analysis framework, this study comprehensively determined the parameter system with a drop hammer mass of 400 kg and drop hammer heights ranging from 0.25 m to 1.5 m, without adjusting parameters for a single study's experiment. This resulted in the inability to fully match parameters with some individual experiments.

(3) There may be differences in the types of boundary constraints between the experiment and the numerical simulation. The numerical model in this study adopts rigid support boundaries, which completely constrain the horizontal displacement and rotation at the ends of the specimen, allowing only vertical deformation. By contrast, the test model may be subject to special constraints, and there may also be discrepancies in the contact conditions between the test specimen and the supporting constraints.

In summary, in engineering applications, a prediction model of "impact height–corrosion rate–peak displacement increase rate" can be established to provide a quantitative basis for the numerical simulation and test design of corroded structures subjected to impact. In addition, the coupling degradation effect of "impact height–corrosion rate" also needs to be incorporated into the deformation and damage reinforcement system of reinforced concrete structures subjected to ship or vehicle collisions.

3.3. Shear Force and Moment

Figure 17 shows the variations in shear force and bending moment across the entire beam section at different moments under a drop hammer impact with a height of 2500 mm. It can be clearly seen from Figure 17 that significant peaks appear in the distributions of shear force (Figure 17a) and bending moment (Figure 17b) at the mid-span of the beam. The shear force and bending moment diagrams at different moments are basically consistent with the distribution law under static loading. However, due to the effect of the impact load and the constraints at the supports, fluctuations occur in bending moment and shear force, and slope changes appear near the supports. In addition, it is worth noting that the shear force and bending moment values along the beam section at the moment of peak impact force are almost all higher than those at the moment of peak displacement. This is because the impact load is instantaneously concentrated on the section at the action point at the moment of peak impact force, leading to a sharp increase in local internal forces. At the moment of peak displacement, the fluctuation range expands to most areas of the beam, meaning that the impact energy has been transmitted and dissipated through the beam, so the peak amplitude of the internal forces of the beam section decreases significantly.

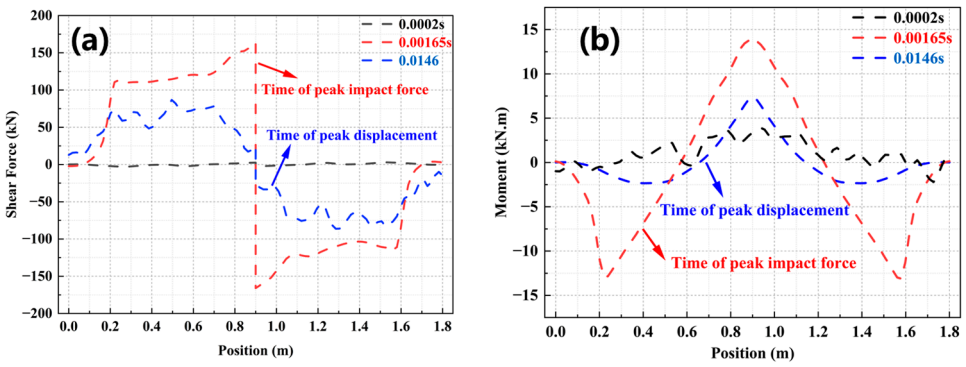

Figure 17. The variations in shear force and bending moment across the entire beam section: (**a**) shear force; (**b**) moment.

Figure 18 displays the time–history curves for shear force and bending moment at the mid-span sections of reinforced concrete beams with different corrosion rates under drop hammer heights of 0.25 m and 0.5 m. By comparing the working conditions of 0.25 m (Figure 18a,c) and 0.5 m (Figure 18b,d), it can be clearly observed that the peak values of shear force and bending moment under the 0.5 m drop hammer height are significantly higher than those under the 0.25 m condition. Under the same drop hammer height, the peak values of shear force and bending moment decrease as the corrosion rate increases, and the occurrence time of the peaks of bending moment and shear force is delayed with the increase in corrosion rate. This can be more obviously observed under the 0.5 m drop hammer height (Figure 18b,d).

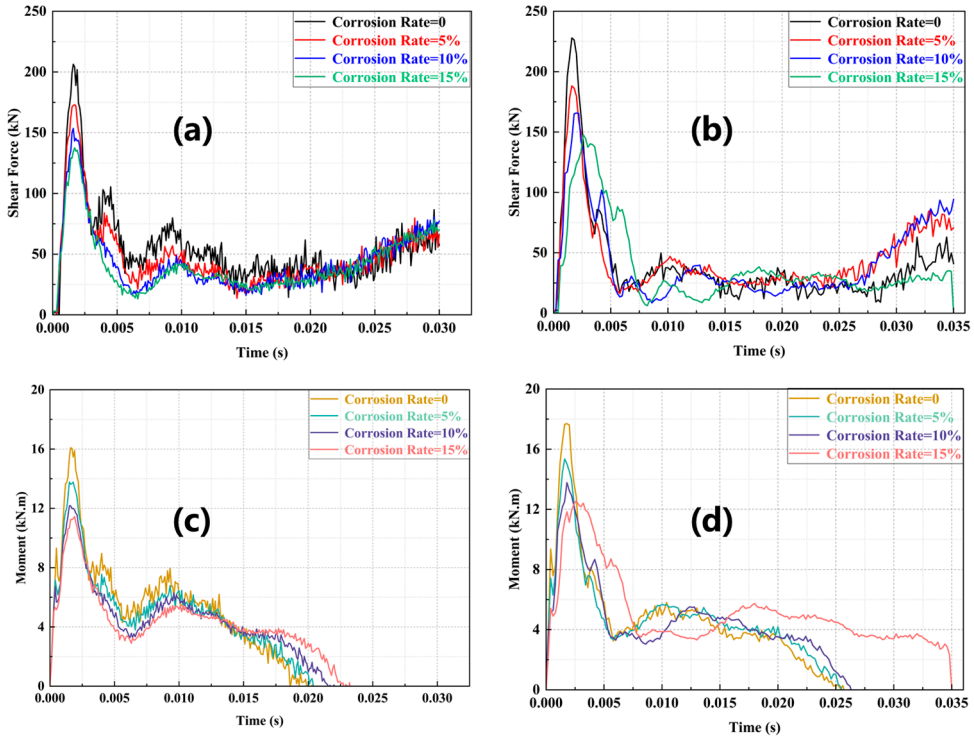

Figure 18. Time–history curves for shear force and bending moment at mid-span section of reinforced concrete beams under different drop hammer heights: (**a**,**c**): 0.25 m; (**b**,**d**): 0.50 m.

It is worth noting that the coupling effect of corrosion and impact is manifested as "higher drop hammer height amplifies the separation impact of corrosion". For example, under the 0.25 m height, the difference between the shear force and bending moment curves for different corrosion rates is relatively small; while under the 0.5 m height, the peak difference and fluctuation difference caused by the corrosion rate expand significantly (e.g., the separation degree between the curve for the 15% corrosion rate and the non-corrosion curve in Figure 17b is much larger than that in Figure 18a). In essence, the high-energy impact at a higher drop hammer height further exposes the stiffness defects and interface bond degradation problems of the corroded structure, causing the degradation degree of internal force response to intensify with the increase in drop hammer height.

Figure 19 further illustrates the distribution of peak shear force and peak bending moment at the mid-span section of RC beams under different drop hammer heights and steel corrosion rates. From Figure 19a,b, it can be clearly observed that at a fixed corrosion rate, both the peak shear force and peak bending moment increase significantly with the rise in drop hammer height. This is because a higher drop hammer height corresponds to greater impact kinetic energy, which results in a higher load intensity trans-

ferred to the beam, thus enhancing the shear force and bending moment responses at the mid-span section.

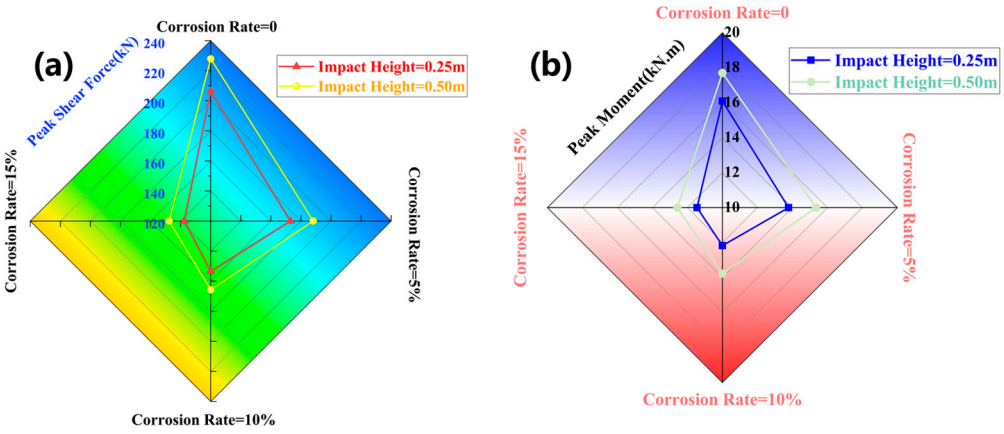

Figure 19. Distribution of peak shear force and peak bending moment at the mid-span section of RC beams under different drop hammer heights and steel corrosion rates: (**a**) shear force; (**b**) moment.

When the drop hammer height is fixed, both the peak shear force and peak bending moment show a downward trend as the corrosion rate increases. The reason is that steel corrosion ultimately leads to gradual degradation in the beam's load-bearing capacity (shear resistance and bending resistance) with the increase in corrosion rate. In addition, a higher drop hammer height can increase the "absolute peak values" of shear force and bending moment, but the increase in corrosion rate will significantly weaken this enhancement effect.

Figure 20 further quantifies the changes in peak shear force and peak bending moment at the mid-span of RC beams under different drop hammer heights and steel corrosion rates. It can be clearly observed from Figure 20 that regardless of the drop hammer height, the degradation rates of peak shear force and peak bending moment increase with the rise in corrosion rate. This indicates that the more severe the corrosion, the more significant the attenuation of the beam's impact resistance. In addition, the drop hammer height has an amplifying effect on the degradation rate: a higher drop hammer height leads to a greater degradation rate at the same corrosion rate.

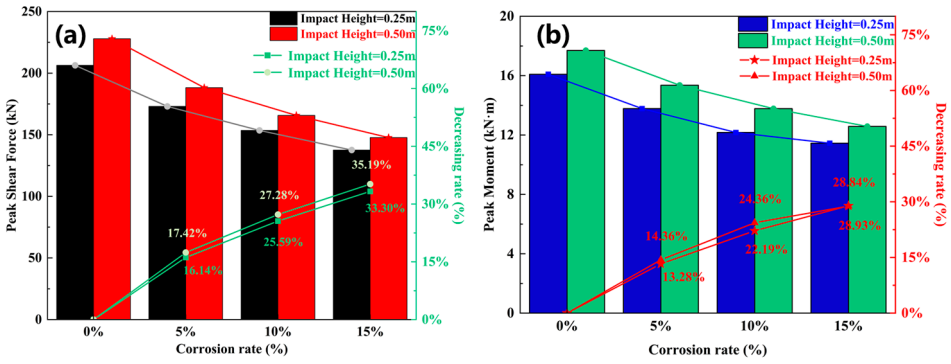

Figure 20. Variation and reduction rate of peak shear force and bending moment at the mid-span of RC beams under different drop hammer heights and steel corrosion rates: (**a**) shear force; (**b**) moment.

By further comparing Figure 20a (shear force) and Figure 20b (bending moment), it can be found that under the same drop height, for every 5% increase in corrosion rate, the peak shear force decreases by an average of 8.2–11.5%, and the peak bending moment decreases by 6.8–9.3%. Notably, the higher the drop height, the greater the magnitude of

this reduction: under a drop height of 0.5 m, the shear force reduction at a 15% corrosion rate (compared to 0% corrosion) reaches 35.19%, while at 0.25 m it is 16.14%.

The mechanical mechanism underlying this difference is as follows: Shear force relies on the synergistic interaction between stirrups and concrete. Corrosion not only causes cross-sectional loss and tensile strength degradation of stirrups but also impairs the bond between concrete and steel reinforcement, leading to a dual weakening of shear resistance. In contrast, bending moment primarily depends on the tensile capacity of longitudinal reinforcement; corrosion affects moment transmission solely through the cross-sectional loss of longitudinal bars, resulting in a more singular degradation pathway.

Consequently, the shear resistance exhibits higher sensitivity to corrosion. This mechanistic insight provides a theoretical basis for determining the prioritization of reinforcement for corroded structures under impact loading.

3.4. Damage

It should be emphasized that the objective of the numerical simulation in this section is to reveal the global damage mechanism of reinforced concrete beams under the coupling effect of corrosion and impact, rather than capturing the mesoscopic crack morphology. The simulation mainly focuses on key macroscopic responses, including the crack propagation trend and evolution of the damage range.

Figure 21 displays the crack evolution processes under drop hammer heights of 0.25 m (left column) and 1.0 m (right column) side by side. By comparing the performances of the 0.25 m and 1.0 m working conditions in the same stage, the following observations can be made:

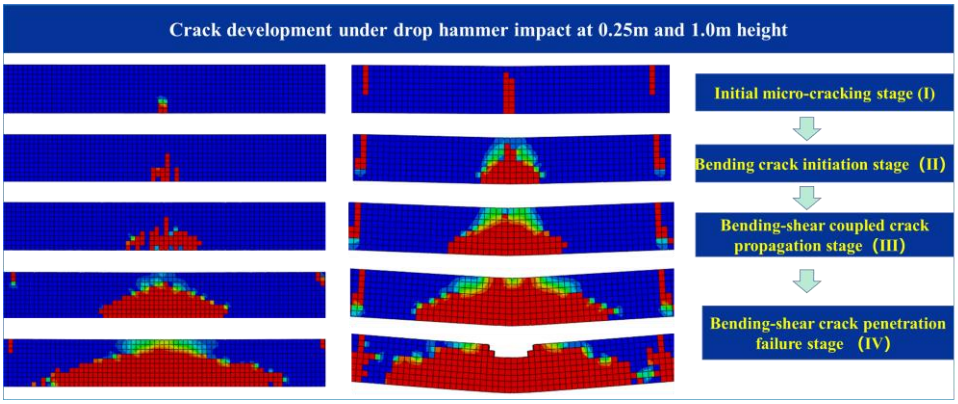

Figure 21. Crack development of reinforced concrete beams under drop hammer impact at 0.25 m and 1.0 m height.

Initial micro-cracking stage (I): For the 0.25 m condition, micro-cracks only appear under the impact zone, while for the 1.0 m condition, stress concentration has already occurred at the beam ends in addition to the impact zone.

In the bending crack initiation stage (II): For the 0.25 m condition, a small area of vertical cracks emerges under the impact zone, whereas for the 1.0 m condition, bending cracks have expanded in clusters and cover a wider area.

In the bending–shear coupled crack propagation/penetration stages (III and IV): The crack propagation speed and penetration degree of the 1.0 m condition are much higher than those of the 0.25 m condition (e.g., in stage IV, the beam under 1.0 m impact has shown obvious deformation, while the 0.25 m condition only reaches crack penetration).

The 0.25 m impact belongs to “low-energy impact”, and its crack development is characterized by “progressive, local dominance”, while the 1.0 m impact belongs to “medium–high-energy impact”, with crack development characterized by “accelerated, full-domain

coupling". The reason for the above failure phenomena is that the increase in drop hammer height accelerates the initiation and initial expansion of bending cracks, showing that the higher the drop hammer height, the shorter the process from "local damage" to "full-domain failure" of cracks. In addition, it is worth noting that in stage IV, the beam under 1.0 m impact shows obvious bending deformation, while the 0.25 m condition shows no significant deformation. The energy of the high drop hammer height is sufficient to bring the beam into a "deformation–failure coupling" state, while the 0.25 m condition only reaches the damage threshold of crack penetration.

Figure 22 presents the comparison of numerical simulation and experimental results for beam damage under different drop hammer heights. By comparing the experimental and simulation results for each working condition (Figure 22a–d), it can be seen that the crack characteristics of the two are basically consistent. This result is also superior to the numerical simulation accuracy and damage distribution rationality reported by Liu et al. [53] (Figure 22e).

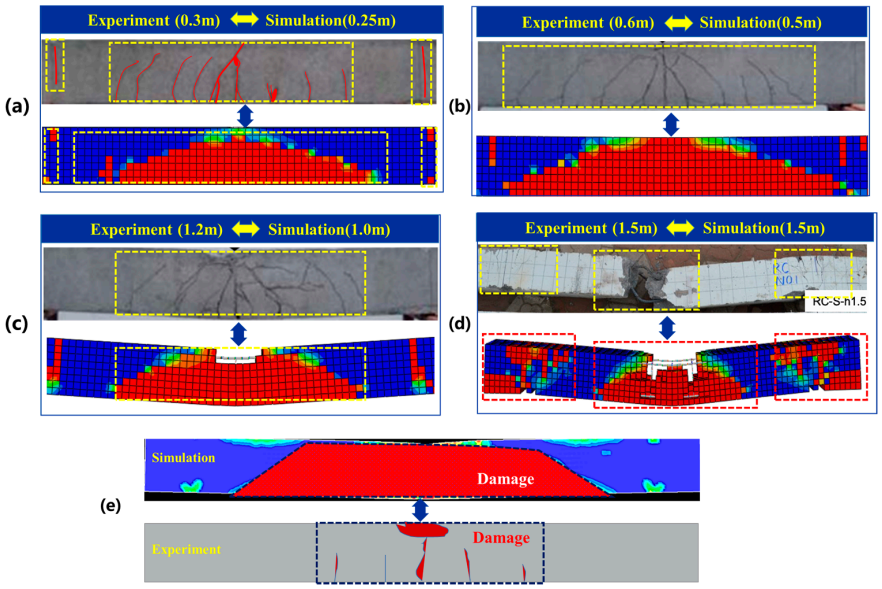

Figure 22. Numerical simulation and experimental [73,74] comparison of beam damage under different drop hammer heights: (**a**) 0.25 m; (**b**) 0.50 m; (**c**) 1.0 m; (**d**) 1.5 m; (**e**) comparison [53].

Under low-energy impacts (Figure 22a,b), both the experiment and simulation show the feature of "local bending cracks dominating the impact zone with concentrated crack distribution"—the distribution of crack elements in the numerical simulation is basically consistent with the actual crack location and morphology in the experiment. Under medium-to-high-energy impacts (Figure 22c,d): the "bending–shear coupled crack clusters and full-domain penetrating cracks" observed in the experiment correspond to large-area damage elements in the simulation. Especially in the d condition, where "concrete spalling and severe damage" occur in the experiment, the numerical simulation method can effectively simulate the crack morphology and damage range under different energy impacts.

In addition, it is worth noting that as the drop hammer height (impact energy) increases, the crack characteristics show an obvious deterioration trend:

From low-to-medium-energy drop hammer impacts, cracks expand from "small-scale bending cracks in the impact zone" to "initial intersection of bending–shear coupled cracks", and the damage area extends from the local region to the mid-span (Figure 22a,b).

From medium-to-high-energy drop hammer impacts, cracks develop from "local coupling" to "full-domain penetration". Concrete spalling occurs in the experiment, and the density and range of damage elements in the corresponding area increase significantly

in the simulation—this reflects the rule that "the higher the impact energy, the denser the cracks and the more severe the damage" (Figure 22b,c,d).

Figure 23 shows the comparison of experimental and numerical simulation results for the failure modes of RC beams with different steel corrosion rates under approximately equal impact energies. It should be emphasized that due to significant discrepancies in the reinforcement, model dimensions, boundary conditions, drop hammer contact area and other aspects between the experiment [72] and the numerical simulation, only a qualitative comparison is conducted between the numerical simulation results for corrosion–impact coupling and the experimental results in Figure 22. It can be clearly observed from Figure 23 that the damage area in the simulation is basically consistent with the crack location in the experiment, and the damage range of the simulation matches well with the actual damage degree of the experiment under different corrosion rates.

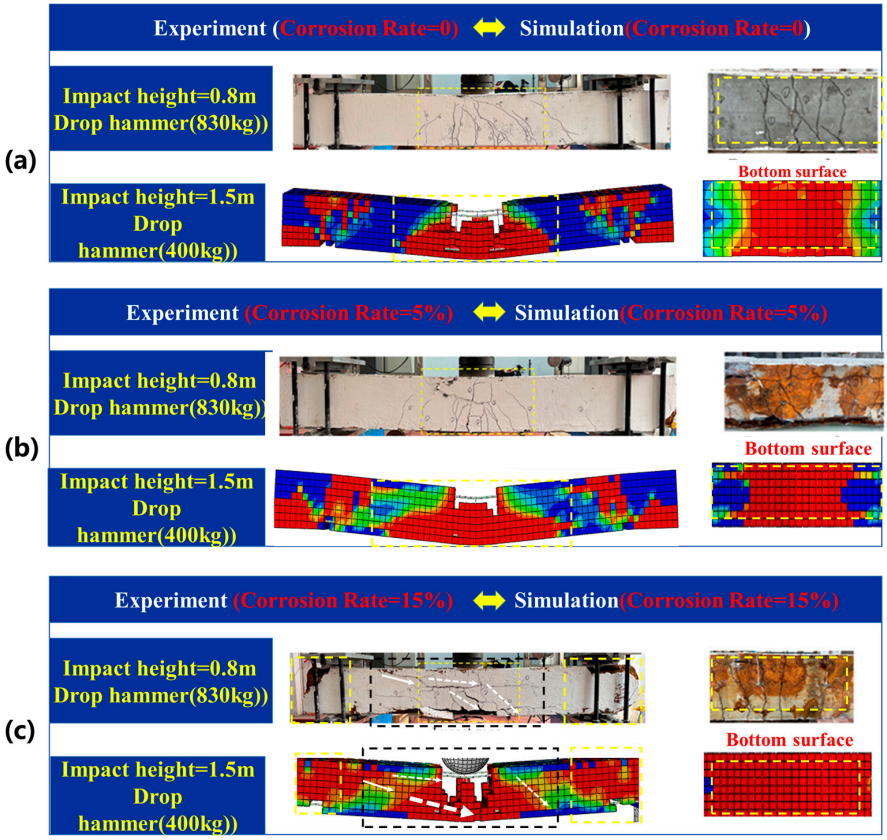

Figure 23. The comparison of experimental [76] and numerical simulation results for the failure modes of RC beams with different steel corrosion rates: (**a**) 0; (**b**) 5%; (**c**) 15%.

It is worth noting that, combined with the experimental and numerical simulation results of Figure 23a (corrosion rate: 0%), Figure 23b (corrosion rate: 5%), and Figure 23c (corrosion rate: 15%), the crack pattern transitions when the corrosion rate is relatively high (15%). The numerical simulation can qualitatively capture the transformation of the damage mode from "dominated by the synergy of flexural–shear cracks" to "dominated by shear cracks + overall brittle failure". This result further verifies the effectiveness of the numerical simulation method employed in this study.

The core objective of this simulation is to reveal the global damage mechanism of the structure rather than the microscopic crack morphology. Local discrepancies exist between the simulated crack distribution and the experimental fracture characteristics, with specific analyses presented as follows:

(1) The reinforcement ratio and cross-sectional dimensions of the experimental specimen are higher than those of the simulated specimen, which endows the steel bars in the experimental specimen with stronger constraint effects and thus leads to more dispersed crack propagation. This is manifested by the occurrence of multiple fine transverse cracks on the beam side in the experiment, while in the simulation, cracks are more concentrated in the mid-span impact zone. Essentially, this discrepancy stems from the regulatory effect of the reinforcement ratio on crack morphology.

(2) There is a difference between the kinetic energy corresponding to the 1.2 m drop height in the numerical simulation and that corresponding to the 1.0 m drop height in the experiment [56]. This energy difference results in more severe concrete spalling in the numerical simulation. The higher impact energy causes the experimental specimen to reach a more severe damage level, with both the crack penetration depth and width being greater than those in the experiment.

(3) Concrete itself exhibits material discreteness. The crack morphologies under the 1.2 m drop height (with a circular arc at the tip of the drop hammer) in the experiment of [56] and the 1.5 m drop height (also with a circular arc at the tip of the drop hammer) in the experiment of [71] show enormous differences (see Figure 22c,d). For the working condition of the 1.5 m drop height in this numerical simulation, the degree of crack penetration and concrete spalling is basically consistent with that in the 1.5 m drop height working condition of the experiment, which verifies the adaptability of the model to different damage levels.

In addition, these discrepancies do not alter the core laws revealed by the study; they only affect the quantitative expression of the damage degree and do not undermine the reliability of the research conclusions. The escalation of the failure mode with increasing corrosion rate is due to the fact that corrosion rate amplifies the failure effect by "weakening the load-bearing capacity". For corroded beams, the bond between steel bars and concrete deteriorates, and their synergistic performance decreases, leading to an expanded damage range and increased damage severity.

Figure 24 further illustrates the evolution law of crack patterns of RC beams under impact loads with different steel corrosion rates. This result is also superior to the numerical simulation accuracy and damage distribution range reported by Liu et al. (Figure 25) [53].

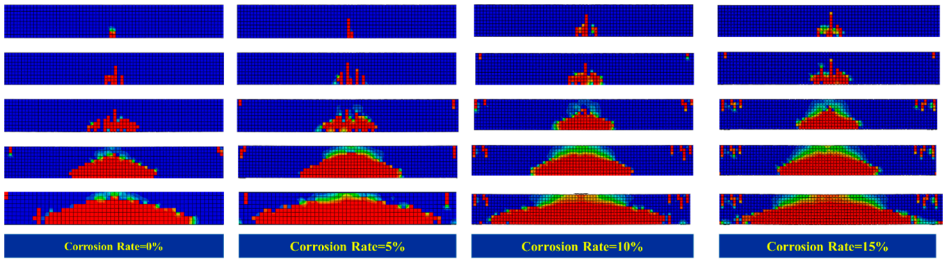

Figure 24. The evolution law of crack patterns of RC beams with different corrosion rates.

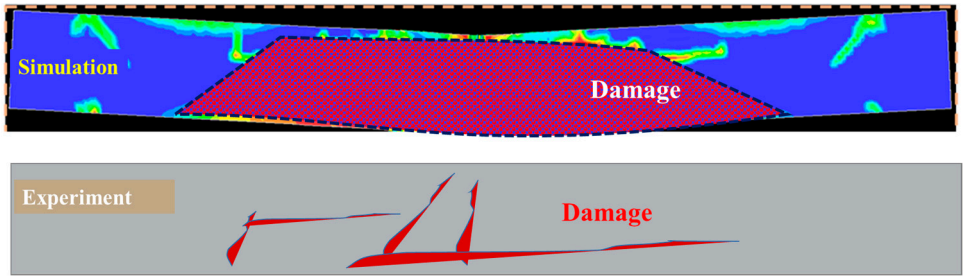

Figure 25. Comparison of damage distribution [53].

As the corrosion rate increases from 0% to 15%, the crack pattern evolves from "localized" to "global":

Corrosion rate = 0% (Column 1): Cracks are dominated by "localized point-like/small-scale areas at the mid-span" (only a small red damage zone appears at the mid-span). This indicates that the impact damage of the non-corroded beam is concentrated near the load application point, and the synergistic restraint between steel bars and concrete effectively limits crack propagation.

Corrosion rate = 5% (Column 2): Cracks extend from the mid-span to the beam ends, forming a "narrow strip-shaped damage zone" (the red area spreads along the beam length). This reflects that the bond between steel bars and concrete begins to degrade, weakening the restraint capacity against cracks.

Corrosion rate = 10% (Column 3): Cracks expand into a "wide strip + local planar damage" (the red area widens, with a yellow transition zone appearing at the edge). At this point, the effective cross-section of the steel bars decreases, leading to more significant tensile stress concentration in the concrete.

Corrosion rate = 15% (Column 4): Cracks evolve into "global planar damage" (the red area covers most of the beam segment), indicating that the synergistic effect between steel bars and concrete is basically invalid, and the integrity of the beam is destroyed.

In summary, under the coupling effect of steel corrosion and drop hammer impact, the damage of RC beams follows the synergistic degradation law of "corrosion exacerbates impact-induced deterioration, and impact amplifies corrosion defects". In the damage characteristic analysis and reinforcement research of practical engineering, damage assessment should take the coupling effect of these two factors into account.

The reinforcement timing should be advanced to the low-corrosion stage. This is because under high corrosion rates, impact loads will rapidly amplify structural defects (such as global crack propagation), and early reinforcement can effectively avoid the risk of brittle failure of a structure in a later stage.

4. Discussion

4.1. Discussion of Mechanism and Results

This section systematically analyzes the coupling mechanism and discusses the reliability of the variation laws of various indicators. By integrating the research of relevant scholars [51–53], the corrosion–impact coupling mechanism of RC members is deeply analyzed and revealed, as illustrated in Figure 26. Chloride ions penetrate and diffuse through concrete pores, triggering electrochemical corrosion on the surface of rebar. The volume expansion of corrosion products (approximately 2–6 times the volume of rebar) generates expansion stress at the rebar–concrete interface, directly damaging the interfacial bonding force; meanwhile, the expansion stress initiates initial micro-cracks in the concrete matrix (i.e., micro-cracks at the aggregate–mortar interface and within the mortar). As a dynamic excitation, the impact load prioritizes acting on these "hidden defects," amplifying the microscale flaws and ultimately causing structural damage. In addition, corrosion degradation reduces the initial energy dissipation capacity of materials. Under impact loading, the energy dissipation curves for concrete and rebar exhibit a "first increasing, then stabilizing" trend; meanwhile, the increase in corrosion rate restricts the "peak energy dissipation interval" of materials. The dynamic loading of impact (i.e., the increase in impact energy) forces the damaged area to dissipate energy through "crack propagation and interfacial friction," leading to failure.

Under the above mechanism, the following laws are formed:

(1) As the corrosion rate increases, the peak force of the member decreases in a stepwise manner. This is essentially the synergistic effect of "rebar cross-sectional

loss + concrete damage accumulation," and the impact load amplifies the damage through "stress concentration and energy increase."

(2) This may occur because the corrosion-induced interfacial micro-cracks directly damage the shear force transfer mechanism of the member (e.g., aggregate interlocking in the inclined section), while the dynamic shear effect of the impact load further accelerates the attenuation of shear force. Eventually, the law that "shear performance is more sensitive to corrosion–impact coupling" is formed.

(3) The mid-span displacement continuously accumulates as the corrosion rate increases, and the damage degree and area also increase with the corrosion rate. A higher corrosion rate leads to more severe initial defects, and the damage amplification effect induced by the impact load becomes stronger.

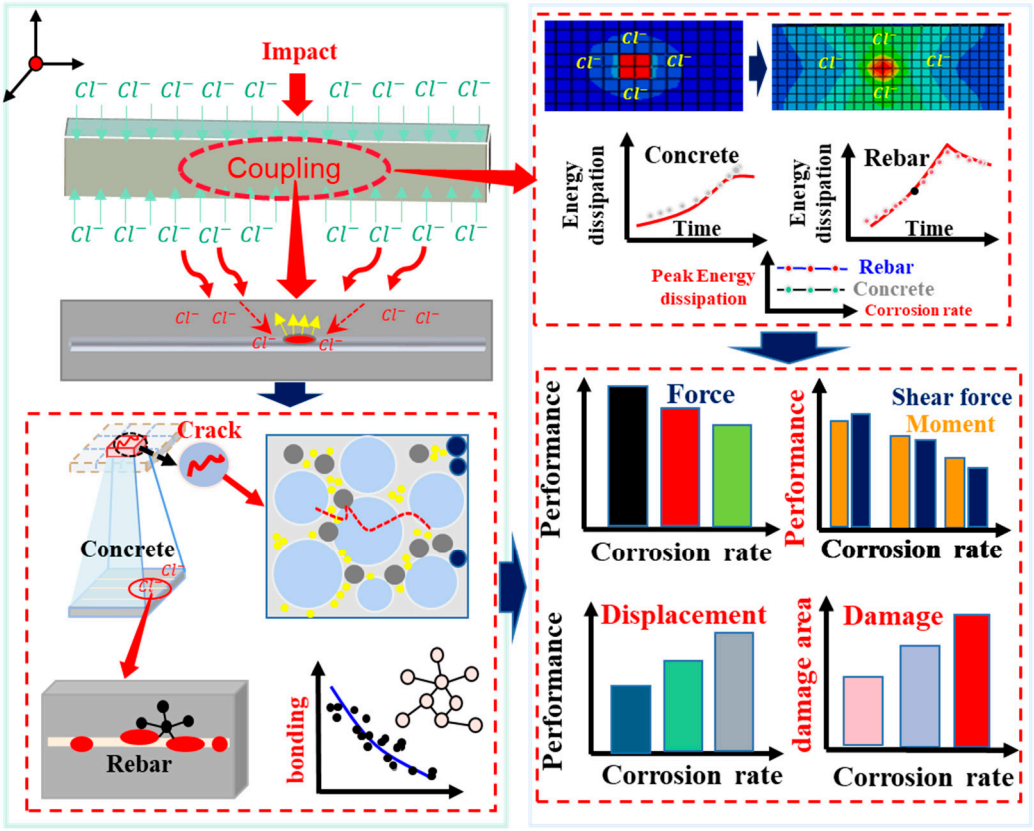

Figure 26. Mechanism and verification of impact–corrosion coupling.

In addition, regarding the peak impact force, the results of this study reveal a clear nonlinear attenuation law: when the corrosion rate reaches 15% and the impact height is 1.5 m, the peak impact force decreases by 49.8% compared with the uncorroded state. This trend is basically consistent with the approximately 42.8% reduction in peak force of test specimen D-L4 (corrosion rate of 11.04%) reported by Kuwahara et al. [77]. Notably, Chen et al. [52] also reported that reinforced concrete columns with a 15% corrosion rate experience an approximately 45% decrease in peak force under low-velocity impact, which is essentially consistent with the attenuation law derived in this study. This cross-validation not only confirms the rationality of the proposed "corrosion rate–peak force" negative correlation law but also verifies the accuracy and reliability of the established numerical model in simulating corrosion–impact coupling effects. Mechanistically, this attenuation phenomenon is essentially the synergistic result of material degradation and structural stiffness reduction induced by corrosion: corrosion causes a loss of steel cross-sectional area and degradation in yield strength [71], while impairing the bond–slip performance

between steel and concrete [57], thereby preventing the structure from effectively resisting impact loads and leading to a significant drop in peak impact force.

In the analysis of mid-span displacement, the peak displacement under a 15% corrosion rate and 1.5 m impact height in this study increases by 35.7% compared with the uncorroded state. This result quantifies the coupled amplification effect of impact height and corrosion rate on displacement: under a low impact height (0.25 m), the increase in peak displacement corresponding to a 15% corrosion rate is only 26.6%, whereas under a high impact height (1.5 m), the increase expands to 35.7%. This indicates that high-energy impact further amplifies the deformation vulnerability of corroded structures. This may be due to the degradation of material and interface properties, which prevents corroded structures from effectively dissipating high impact energy through the synergistic deformation of steel and concrete, so that instead they can only absorb energy through larger displacements, resulting in a more significant increase in peak displacement.

In terms of shear force and bending moment analysis, this study reveals a key finding: "shear performance is more sensitive to corrosion–impact coupling effects". At a 15% corrosion rate, the shear force decreases by 35.19%, while the bending moment decreases by 28.93%. The high sensitivity of shear performance is determined by the inherent force-bearing mechanism of shear resistance. The shear resistance of reinforced concrete structures relies on the synergistic effect of stirrups, concrete, and steel–concrete bonding [28]. Corrosion not only causes a loss of stirrup cross-sectional area and degradation in tensile strength but also impairs the bond performance between steel and concrete, leading to dual weakening of shear resistance. This mechanistic difference is further supported by the relevant literature: the propagation rate of shear cracks after corrosion is 1.8 times greater than that of flexural cracks [77]. Chen et al. [52] and Liu et al. [53] also confirmed in their studies on corroded reinforced concrete columns and beams that the reduction in shear force is consistently greater than that in bending moment. These consistent research results collectively verify the scientific validity of the conclusion that "shear performance is more sensitive to corrosion" in this study.

Regarding failure mode and crack morphology, the numerical simulation results of this study are highly consistent with the typical failure characteristics of reinforced concrete beams under corrosion–impact coupling effects. Reinforced concrete beams with a 15% corrosion rate exhibit "concrete spalling + full-section through cracks" after impact, which is a similar finding to the experimental failure morphology of corroded reinforced concrete piers reported by Wu et al. [76] and the failure characteristics of corroded reinforced concrete beams under drop hammer impact observed by Kuwahara et al. [77]. Specifically, as the corrosion rate increases, the crack morphology evolves from localized mid-span cracks (0% corrosion rate) to through cracks (15% corrosion rate), and the failure mode transforms from flexural–shear coupled failure to shear-dominated brittle failure. The consistency between the simulation results and experimental observations in the literature fully confirms that the established numerical model can accurately capture the damage evolution and failure mode transformation of corroded reinforced concrete structures under impact loads.

In summary, through in-depth mechanism research and multi-indicator quantification, this study fully explains the corrosion–impact coupling mechanism, providing key mechanistic support for the "service life prediction and protective design" of RC members in corrosion–dynamic load coupling environments such as marine and port engineering.

4.2. Practical Significance, Limitations and Future Research Suggestions

This study focuses on reinforced concrete (RC) structural members often exposed to the harsh environment of coupled corrosion and impact, which holds significant engineering

significance. At the design stage, the coupling effect of corrosion and impact should be considered to reasonably determine the corrosion rate control standard and impact load safety factor. For instance, for offshore structures in high-corrosion environments, the corrosion rate should be controlled within 5% as much as possible to avoid excessive degradation in structural performance. During the maintenance phase, regular inspections of the structural corrosion status are essential. When the corrosion rate reaches 10%, timely reinforcement measures should be implemented to prevent brittle failure under impact loads. In the reinforcement stage, priority should be given to strengthening the shear resistance system—for instance, increasing the stirrup ratio in the impact zone or adopting ultra-high-performance concrete (UHPC) wrapping technology—to enhance the structural shear capacity and reduce the risk of shear failure.

However, this study has obvious limitations. It only focuses on the coupling effect of chloride-induced corrosion and impact loads, without considering the influence of multiple environmental factors (e.g., concrete carbonation, temperature fluctuations, and sulfate attack) on the corrosion process and structural performance. In actual marine environments, RC structures are often subjected to the combined action of multiple environmental factors, leading to more complex corrosion mechanisms and structural performance degradation laws. Additionally, this study only investigates the dynamic performance of RC beams under the coupling of corrosion and impact, and the research results may not be directly applicable to other types of RC structures (e.g., columns, slabs, and shells). Different structural types have distinct force mechanisms and damage characteristics under impact loads, and the impact of corrosion on their dynamic performance may also vary. In addition, this study does not consider the characteristics of steel pitting corrosion and the uneven spatial distribution of corrosion that are prevalent in actual marine environments. In particular, pitting corrosion tends to occur at local positions of steel bars, which significantly reduces the effective cross-sectional area of the bars and induces stress concentration, thereby accelerating crack initiation and structural degradation [53]. The corrosion model adopted in this study cannot fully capture the processes of localized damage evolution, transient crack propagation, and uneven mechanical property degradation of structures under corrosion–impact coupled loads.

To address these limitations, future research can utilize machine learning methods to establish prediction models for structural dynamic performance under the coupling of corrosion and impact, enabling rapid and accurate prediction of structural performance degradation under different working conditions. Meanwhile, it is necessary to conduct experimental and numerical simulation studies on the coupling effect of multiple environmental factors (corrosion + carbonation + temperature) and impact loads, exploring the influence of multiple factors on the corrosion process and structural dynamic performance. Additionally, the research scope should be expanded to other types of RC structures, such as columns and slabs, with comparative analysis of the dynamic performance of different structural types under the coupling of corrosion and impact to provide a more comprehensive theoretical basis for engineering practice. Targeted reinforcement technology research can also be carried out for the performance degradation of corroded RC structures under impact loads. For example, the reinforcement effect of new materials such as UHPC and fiber-reinforced polymers (FRPs) on corroded RC structures under impact loads can be studied to determine the optimal reinforcement scheme. Simultaneously, the durability and long-term performance of reinforced structures should be investigated to ensure the long-term safety and reliability of structures in harsh environments.

5. Conclusions

This study established a refined three-dimensional numerical model of drop hammer-reinforced concrete (RC) beams using ABAQUS-6.14 software, fully considering the strain rate effects of steel bars and concrete, the bond–slip behavior at the steel–concrete interface, and the constitutive model of corroded steel bars. The validity of the model was verified by comparing it with experimental data from the existing literature. Subsequently, parametric simulations were conducted to systematically investigate the dynamic responses and damage mechanisms of RC beams under the coupling action of different corrosion rates (0%, 5%, 10%, and 15%) and impact loads corresponding to various drop heights (0.25 m, 0.5 m, 1.0 m, and 1.5 m). The main conclusions are as follows:

(1) The established numerical model exhibits high reliability in simulating the dynamic responses and damage characteristics of corroded reinforced concrete (RC) beams under impact loading. The simulation results are basically consistent with the experimental laws, verifying its effectiveness for corrosion–impact coupling analysis.

(2) Corrosion significantly impairs structural impact resistance, leading to a decrease in peak impact force and an increase in mid-span displacement. This degradation effect is further amplified with the increase in impact height, presenting a notable coupling amplification law.

(3) The shear performance of RC beams is more sensitive to corrosion–impact coupling than flexural performance. At a corrosion rate of 15%, the shear force decreases by 35.19%, while the bending moment decreases by 28.93%. This difference stems from the dual weakening of the stirrup function and steel–concrete bond induced by corrosion, which affects shear performance.

(4) Corrosion drives the evolution of cracks from a localized distribution to a global distribution, and a higher drop height accelerates the transition of the failure mode toward brittle shear failure. When the corrosion rate reaches 15% and the drop height is 1.5 m, the structure transforms from flexural–shear coupled failure to shear-dominated brittle failure, characterized by concrete spalling and full-section through cracks.

(5) The corrosion–impact coupling mechanism forms a positive feedback cycle: corrosion induces initial micro-cracks and material degradation, impact loads amplify these defects into macro-damage, and the expanded cracks further facilitate the penetration of corrosion media. This synergistic effect results in nonlinear degradation in structural performance, the degree of which exceeds the superposition of the individual effects of corrosion and impact.

This study provides insights into the corrosion–impact coupling behavior of RC beams but has the following limitations that require further research: it only focuses on the single coupling action of "corrosion–impact" and does not involve the influence of the coupling of multiple environmental factors (such as concrete carbonation cycles and temperature fluctuations) on corrosion development and material performance. In addition, the simplified treatment of concrete strength reduction in the simulation fails to cover the non-uniform and localized characteristics of corrosion in actual marine structures, as well as the transient response law of concrete cracks under dynamic loads. This may lead to discrepancies between the refined quantification of the coupling effect and engineering practice.

Author Contributions: X.L.: Conceptualization, Methodology, Formal analysis, Data curation, Writing—original draft. Y.Z. (Yonglai Zheng): Conceptualization, Methodology, Writing—review and editing. T.P.: Funding acquisition, Methodology, Supervision. Y.Z. (Yubao Zhou): Resources,

Writing—review and editing. Y.W. and Y.C.: Investigation, Resources. All authors have read and agreed to the published version of the manuscript.

Funding: This research was funded by the Early Career Youth Science and Technology Talent Training Program of Jiangxi Province (No. 20244BCE52161).

Data Availability Statement: The data are available from the corresponding author upon reasonable request.

Conflicts of Interest: The authors declare no conflicts of interest.

References

1. Zhao, Y.; Xu, X.; Wang, Y.; Dong, J. Characteristics of pitting corrosion in an existing reinforced concrete beam exposed to marine environment. *Constr. Build. Mater.* **2020**, *234*, 117392. [CrossRef]
2. Ma, Y.; Zhang, J.; Wang, L.; Liu, Y. Probabilistic prediction with Bayesian updating for strength degradation of RC bridge beams. *Struct. Saf.* **2013**, *44*, 102–109. [CrossRef]
3. Luo, Q.; Xu, G.; Zhao, J.; Wang, Q. Evolution characteristics of secondary tensile mechanical properties of corroded rebars. *Structures* **2021**, *34*, 3478–3486. [CrossRef]
4. Jin, L.; Li, Y.X.; Zhang, R.B.; Du, X.L. Mesoscopic investigation on seismic performance of corroded reinforced concrete columns. *Earthq. Eng. Eng. Vib.* **2022**, *21*, 969–985. [CrossRef]
5. Han, S.J.; Ju, H.; Lee, D. Practical approach for estimating flexural strengths of corroded RC members considering bond strength degradation. *Structures* **2022**, *39*, 808–820. [CrossRef]
6. Anania, L.; Badalà, A.; D'Agata, G. Damage and collapse mode of existing post tensioned precast concrete bridge: The case of Petrulla viaduct. *Eng. Struct.* **2018**, *162*, 226–244. [CrossRef]
7. Babaee, M.; Castel, A. Chloride diffusivity, chloride threshold, and corrosion initiation in reinforced alkali-activated mortars: Role of calcium, alkali, and silicate content. *Cement Concr. Res.* **2018**, *111*, 56–71. [CrossRef]
8. Xie, Y.; Zhan, T.; Fan, Y.; Chen, J.; Xie, Z. Research on overall bearing characteristics of high-piled wharf under horizontal load. *IOP Conf. Ser. Earth Environ. Sci.* **2021**, *768*, 12170. [CrossRef]
9. Xie, Y.; Liu, C.; Gao, S.; Tang, J.; Chen, Y. Lateral load bearing capacity of offshore high-piled wharf with batter piles. *Ocean Eng.* **2017**, *142*, 377–387. [CrossRef]
10. Wang, W.; Fang, Z.C.; Fu, J.H.; Wang, S.; Zhou, R.X. Damage analyses of the main pylon of a suspension bridge under ship impact using fiber beam elements. *Ocean Eng.* **2025**, *322*, 120459. [CrossRef]
11. Wardhana, K.; Hadipriono, F.C. Analysis of recent bridge failures in the United States. *J. Perform. Constr. Fac.* **2003**, *17*, 144–159. [CrossRef]
12. Xie, L.; Su, L.; Wan, H.-P.; Wang, J.; Bi, J.; Ling, X. Experimental study on dynamic response of pile-supported wharf under wave and ship berthing collision. *Appl. Ocean Res.* **2023**, *135*, 103561. [CrossRef]
13. Wang, C.Q.; Liu, Q.; Gao, J.; Chen, Z. Ship load response test and structural bearing capacity assessment of high-piled wharfs. *J. Pearl River* **2020**, *41*, 60–64.
14. Jiang, H.; Wang, J.J.; Chorzepa, M.G.; Zhao, J.D. Numerical investigation of progressive collapse of a multispan continuous bridge subjected to vessel collision. *J. Bridge Eng.* **2017**, *22*, 04017008. [CrossRef]
15. Shen, D.J.; Sun, W.B.; Fan, W.; Huang, X.; He, Y.B. Behavior and analysis of simply supported bridges under vessel side collisions: Implications from collapse of the Taiyangbu Bridge. *J. Bridge Eng.* **2022**, *27*, 04022076. [CrossRef]
16. Duan, M.; Miao, J.; Wu, J.; Dong, F. Reliability assessment approach for fire resistance performance of prestressed steel-concrete box girder bridges. *Fire* **2023**, *6*, 472. [CrossRef]
17. Duan, M.; Xue, J.; Wang, X.; Wu, Y.; Tao, H. Experimental study on shear performance of perfobond steel plate in ultra-high performance concrete (UHPC)-normal concrete (NC) connection. *Structures* **2024**, *66*, 106783. [CrossRef]
18. Wu, H.; Xu, F.; Li, B.; Gao, Q. Study on expansion rate of steel slag cement-stabilized macadam based on BP neural network. *Materials* **2024**, *17*, 3558. [CrossRef]
19. Apostolopoulos, C.A. The influence of corrosion and cross-section diameter on the mechanical properties of b500 c steel. *J. Mater. Eng. Perform.* **2009**, *18*, 190–195. [CrossRef]
20. Castel, A.; François, R.; Arliguie, G. Mechanical behaviour of corroded reinforced concrete beams-Part 2: Bond and notch effects. *Mater. Struct.* **2000**, *33*, 545–551. [CrossRef]
21. Gu, X.; Zhang, W.; Shang, D.; Wang, X.G. Flexural behavior of corroded reinforced concrete beams. In *Earth and Space 2010: Engineering, Science, Construction, and Operations in Challenging Environments*; American Society of Civil Engineers: Reston, VA, USA, 2010; pp. 3545–3552.

22. El Maaddawy, T.A.; Soudki, K.A. Effectiveness of impressed current technique to simulate corrosion of steel reinforcement in concrete. *J. Mater. Civ. Eng.* **2003**, *15*, 41–47. [CrossRef]
23. Padmarajaiah, S.; Ramaswamy, A. A finite element assessment of flexural strength of prestressed concrete beams with fiber reinforcement. *Cem. Concr. Compos.* **2002**, *24*, 229–241. [CrossRef]
24. Francois, R.; Maso, J. Effect of damage in reinforced concrete on carbonation or chloride penetration. *Cem. Concr. Res.* **1988**, *18*, 961–970. [CrossRef]
25. Konin, A.; Francois, R.; Arliguie, G. Penetration of chlorides in relation to the microcracking state into reinforced ordinary and high strength concrete. *Mater. Struct.* **1998**, *31*, 310–316. [CrossRef]
26. Yoon, S.; Wang, K.; Weiss, W.J.; Shah, S.P. Interaction between loading, corrosion, and serviceability of reinforced concrete. *Mater. J.* **2000**, *97*, 637–644.
27. Pham, T.T.; Nguyen, N.T.; Nguyen, T.-T.T.; Nguyen, N.L. Numerical analysis of the shear behavior for steel fiber reinforced concrete beams with corroded reinforcing bars. *Structures* **2023**, *57*, 105081. [CrossRef]
28. Li, Y.; Sun, Z.; Li, Y.; Zhu, W.; Zheng, H.; Zheng, S. Exploring the shear performance and predictive shear capacity of corroded RC columns utilizing the modified compression-field theory: An investigative study. *Eng. Struct.* **2024**, *302*, 117390. [CrossRef]
29. Guo, A.X.; Li, H.T.; Ba, X.; Guan, X.C.; Li, H. Experimental investigation on the cyclic performance of reinforced concrete piers with chloride-induced corrosion in marine environment. *Eng. Struct.* **2015**, *105*, 1–11. [CrossRef]
30. Yuan, W.; Guo, A.X.; Li, H. Experimental investigation on the cyclic behaviors of corroded coastal bridge piers with transfer of plastic hinge due to non-uniform corrosion. *Soil Dyn. Earthq. Eng.* **2017**, *102*, 112–123. [CrossRef]
31. Chinnasamy, Y.; Joanna, P.S.; Kothanda, K.; Gurupatham, B.G.A.; Roy, K. Behavior of Pultruded Glass-Fiber-Reinforced Polymer Beam-Columns Infilled with Engineered Cementitious Composites under Cyclic Loading. *J. Compos. Sci.* **2022**, *6*, 338. [CrossRef]
32. Kashani, M.M.; Lowes, L.N.; Crewe, A.J.; Alexander, N.A. Nonlinear fibre element modelling of RC bridge piers considering inelastic buckling of reinforcement. *Eng. Struct.* **2016**, *116*, 163–177. [CrossRef]
33. Cheng, H.; Li, H.N.; Biondini, F.; Wang, D.S.; Zou, Y. Strain penetration effect on cyclic response of corroded RC columns. *Eng. Struct.* **2021**, *243*, 112653. [CrossRef]
34. Xu, J.G.; Hong, W.; Zhang, J.; Hou, S.T.; Wu, G. Seismic performance assessment of corroded RC columns based on data-driven machine-learning approach. *Eng. Struct.* **2022**, *255*, 113936. [CrossRef]
35. Miao, Z.; Yuan, H.; Liu, Y.; Geng, X. Seismic performance analysis of coastal reinforced concrete frames considering the pitting corrosion in the longitudinal reinforcement bars. *J. Build. Eng.* **2024**, *90*, 109478. [CrossRef]
36. Meda, A.; Mostosi, S.; Rinaldi, Z.; Riva, P. Experimental evaluation of the corrosion influence on the cyclic behaviour of RC columns. *Eng. Struct.* **2014**, *76*, 112–123. [CrossRef]
37. Li, D.W.; Wei, R.; Xing, F.; Sui, L.L.; Zhou, Y.W.; Wang, W.Y. Influence of non-uniform corrosion of steel bars on the seismic behavior of reinforced concrete columns. *Constr. Build. Mater.* **2018**, *167*, 20–32. [CrossRef]
38. Li, J.; Kang, Z.; Yu, G.; Wang, S.; Wu, M.; Bu, L.; Farooq, A.; Kai, C. Dynamic Response and Failure Mode of Reinforced Concrete Beams Subjected to Impact. *Buildings* **2025**, *15*, 3250. [CrossRef]
39. Wu, J.; Ye, F.; Yang, J.; Xu, J. Dynamic Response and Residual Bearing Capacity of Corroded RC Piers Under Rockfall Impact. *Buildings* **2025**, *15*, 2592. [CrossRef]
40. Tran, D.T.; Lee, H.-S.; Singh, J.K.; Yang, H.-M.; Jeong, M.-G.; Yan, S.; Ibrahim, I.S.; Ariffin, M.A.B.M.; Le, A.-T.; Singh, A.K. Effects of Hybrid Corrosion Inhibitor on Mechanical Characteristics, Corrosion Behavior, and Predictive Estimation of Lifespan of Reinforced Concrete Structures. *Buildings* **2025**, *15*, 1114. [CrossRef]
41. Zhu, X.; Zhang, Q.; Zhang, D.J.; Du, Y.F.; Zhang, Q. Experimental and numerical study on the dynamic response of steel-reinforced concrete composite members under lateral impact. *Thin-Walled Struct.* **2021**, *169*, 108477. [CrossRef]
42. Zhu, X.; Zhao, P.J.; Tian, Y.; Wang, R. Experimental study of RC columns and composite columns under low-velocity impact. *Thin-Walled Struct.* **2021**, *160*, 107374. [CrossRef]
43. Pham, T.M.; Hao, H. Effect of the plastic hinge and boundary conditions on the impact behavior of reinforced concrete beams. *Int. J. Impact Eng.* **2017**, *102*, 74–85. [CrossRef]
44. Pham, T.M.; Hao, H. Plastic hinges and inertia forces in RC beams under impact loads. *Int. J. Impact Eng.* **2017**, *103*, 1–11. [CrossRef]
45. Pham, T.M.; Hao, H. Influence of global stiffness and equivalent model on prediction of impact response of RC beams. *Int. J. Impact Eng.* **2018**, *113*, 88–97. [CrossRef]
46. Li, H.W.; Chen, W.S.; Hao, H. Factors influencing impact force profile and measurement accuracy in drop weight impact tests. *Int. J. Impact Eng.* **2020**, *145*, 103688. [CrossRef]
47. Li, M.; Gao, Y.; Wang, C.; Li, Y.; Fan, T. Impact Resistance Test and Numerical Simulation Study of Scrap Steel Fiber Rubber Concrete. *Buildings* **2025**, *15*, 2857. [CrossRef]

48. Wang, Y.; Gu, X.; Xia, Y. Dynamic Response Analysis of Corroded Pipelines Containing $SCCO_2$ under Rockfall Impact. *Processes* **2024**, *12*, 2201. [CrossRef]
49. Cheng, J.S.; Wen, H.M. Effect of impact velocity on the failure modes of a RC beam. *Int. J. Impact Eng.* **2022**, *160*, 104061. [CrossRef]
50. Daneshvar, K.; Moradi, M.; Ahmadi, K.; Hajiloo, H. Strengthening of corroded reinforced concrete slabs under multi-impact loading: Experimental results and numerical analysis. *Constr. Build. Mater.* **2021**, *284*, 122650. [CrossRef]
51. Tamai, H.; Sonoda, Y.; Bolander, J.E. Impact resistance of RC beams with reinforcement corrosion: Experimental observations. *Constr. Build. Mater.* **2020**, *263*, 120638. [CrossRef]
52. Chen, T.; Luo, Y.; Shen, Y.; Zhang, L. Dynamic behaviors of corroded RC column under low-velocity impact loading. *Ocean Eng.* **2025**, *324*, 120679. [CrossRef]
53. Liu, Y.; Hao, Y.; Hao, H.; Li, H.; Zhou, Y. Dynamic response of concrete beams considering spatial variability of pitting corrosion damages subjected to impact loads. *Eng. Struct.* **2025**, *332*, 120026. [CrossRef]
54. Molina, F.J.; Alonso, C.; Andrade, C. Cover cracking as a function of rebar corrosion: Part 2-Numerical model. *Mater. Struct.* **1993**, *26*, 532–548. [CrossRef]
55. Fujikake, K.; Mori, K.; Uebayashi, K.; Ohno, T.; Mizuno, J. Constitutive model for concrete materials with high-rates of loading under tri-axial compressive stress states. In Proceedings of the 3rd International Conference on Concrete Under Severe Conditions of Environment and Loading, Vancouver, BC, Canada, 18–20 June 2001.
56. Malvar, L.J. Review of static and dynamic properties of steel reinforcing bars. *Mater. J.* **1998**, *95*, 609–616.
57. Lin, H.; Zhao, Y.; Yang, J.; Feng, P.; Ozbolt, J.; Ye, H. Effects of the corrosion of main bar and stirrups on the bond behavior of reinforcing steel bar. *Constr. Build. Mater.* **2019**, *225*, 13. [CrossRef]
58. Lee, J.; Fenves, G.L. Plastic-damage model for cyclic loading of concrete structures. *J. Eng. Mech.* **1998**, *124*, 892. [CrossRef]
59. *GB 50010-2010*; Code for Design of Concrete Structures. China Architecture & Building Press: Beijing, China, 2010.
60. Hanjari, K.Z.; Kettil, P.; Lundgren, K. Analysis of mechanical behavior of corroded reinforced concrete structures. *ACI Struct. J.* **2011**, *108*, 532–541. [CrossRef]
61. Ross, C.A.; Thompson, P.Y.; Tedesco, J.W. Split-Hopkinson pressure-bar tests on concrete and mortar in tension and compression. *ACI Mater. J.* **1989**, *86*, 475–481.
62. Coronelli, D.; Gambarova, P. Structural assessment of corroded reinforced concrete beams: Modeling guidelines. *J. Struct. Eng.* **2004**, *130*, 1214–1224. [CrossRef]
63. Vu, N.S.; Yu, B.; Li, B. Prediction of strength and drift capacity of corroded reinforced concrete columns. *Constr. Build. Mater.* **2016**, *115*, 304–318. [CrossRef]
64. Li, J.B.; Markeset, G.; Kioumarsi, M. Nonlinear FEM simulation of structural performance of corroded RC columns subjected to Axial Compression. *Nord. Concr. Res.* **2017**, *57*, 15–22.
65. Campione, G.; Cannella, F.; Minafo, G. A simple model for the calculation of the axial load-carrying capacity of corroded RC columns. *Mater. Struct.* **2016**, *49*, 1935–1945. [CrossRef]
66. Campione, G.; Cannella, F.; Cavaleri, L.; Ferrotto, M.F. Moment-axial force domain of corroded RC columns. *Mater. Struct.* **2017**, *50*, 21. [CrossRef]
67. Capé, M. *Residual Service-Life Assessment of Existing R/C Structures*; Chalmers University of Technology: Gothenburg, Sweden, 1999.
68. Li, S.Y.; Zhao, J.C. Study on the degradation law of mechanical properties of corroded steel bars in salt lake environment. *Exp. Technol. Manag.* **2019**, *36*, 50–54. (In Chinese)
69. Zhang, W.P.; Shang, D.F.; Gu, Y.L. Study on the stress-strain relationship of corroded steel bars. *J. Tongji Univ. Nat. Sci. Ed.* **2006**, *34*, 586–592. (In Chinese)
70. Kartopu, G.; Turkay, D.; Ozcan, C.; Hadibrata, W.; Aurang, P.; Yerci, S.; Unalan, H.; Barrioz, V.; Qu, Y.; Bowen, L.; et al. Photovoltaic performance of CdS/CdTe junctions on ZnO nanorod arrays. *Sol. Energy Mater. Sol. Cells* **2018**, *176*, 100–108. [CrossRef]
71. Wang, X.H.; Liu, X.L. Modeling the flexural carrying capacity of corroded RC beam. *J. Shanghai Jiaotong Univ.* **2008**, *13*, 129–135. [CrossRef]
72. Wu, Q.; Yuan, Y.S. Experimental study on the deterioration of mechanical properties of corroded steel bars. *China Civ. Eng. J.* **2008**, *41*, 42–47. (In Chinese)
73. Fujikake, K.; Li, B.; Soeun, S. Impact response of reinforced concrete beam and its analytical evaluation. *J. Struct. Eng.* **2009**, *135*, 938–950. [CrossRef]
74. Wei, J.; Li, J.; Wu, C. An experimental and numerical study of reinforced conventional concrete and ultra-high performance concrete columns under lateral impact loads. *Eng. Struct.* **2019**, *201*, 109822. [CrossRef]
75. Nagao, T.; Lu, P. A simplified reliability estimation method for pile-supported wharf on the residual displacement by earthquake. *Soil Dyn. Earthq. Eng.* **2020**, *129*, 105904. [CrossRef]

76. Wu, H.; Liu, X.; Cheng, Y.H.; Chen, T.L. Dynamic behaviors of bridge with corroded RC piers under barge collisions. *Eng. Struct.* **2024**, *319*, 118843. [CrossRef]
77. Kuwahara, I.; Tama, H.; Sonoda, Y. Experimental study on impact load resistance of RC beam with corroded reinforcement. *MATEC Web Conf.* **2016**, *47*, 02004. [CrossRef]